

Single particle trajectories reveal active Endoplasmic Reticulum luminal flow

David Holcman^{1, †, *}, Pierre Parutto^{1, †}, Joseph E. Chambers², Marcus Fantham³, Laurence J. Young³, Stefan J. Marciniak², Clemens F. Kaminski³, David Ron² & Edward Avezov^{2, 4 *}

¹ Group of applied Mathematics and Computational Biology, Ecole Normale Supérieure, IBENS, 46 rue d'Ulm, 75005 Paris, France

² Cambridge Institute for Medical Research, University of Cambridge, CB2 0XY, United Kingdom

³ Department of Chemical Engineering and Biotechnology, University of Cambridge, Cambridge CB3 0AS, United Kingdom

⁴ UK Dementia Research Institute at University of Cambridge, University of Cambridge, Department of Clinical Neurosciences, Cambridge CB2 0AH, United Kingdom

[†] Equal contribution

*Address correspondence to: Edward Avezov at ea347@cam.ac.uk and D. Holcman at david.holcman@ens.fr

Abstract:

The Endoplasmic Reticulum (ER), a network of membranous sheets and pipes, supports functions encompassing biogenesis of secretory proteins and delivery of functional solutes throughout the cell^{1,2}. Molecular mobility through the ER network enables these functionalities, but diffusion alone is not sufficient to explain luminal transport across supramicron distances. Understanding the ER structure-function relationship is critical in light of mutations in ER morphology regulating proteins that give rise to neurodegenerative disorders^{3,4}. Here, super-resolution microscopy and analysis of single particle trajectories of ER luminal proteins revealed that the topological organization of the ER correlates with distinct trafficking modes of its luminal content: with a dominant diffusive component in tubular junctions and a fast flow component in tubules. Particle trajectory orientations resolved over time revealed an alternating current of the ER contents, whilst fast ER super-resolution identified energy-dependent tubule contraction events at specific points as a plausible mechanism for generating active ER luminal flow. The discovery of active flow in the ER has implications for timely ER content distribution throughout the cell, particularly important for cells with extensive ER-containing projections such as neurons.

The Endoplasmic Reticulum (ER) is a contiguous network of membranous sheet-like reservoirs and tubes extending throughout the cell. Maintained by membrane-shaping proteins^{1,2}, this morphology supports the distribution of ER luminal content to distant sites. ER-content distribution rate affects the efficiency of ER-mediated intracellular connectivity. Perturbation of this fundamental process may contribute to diseases caused by mutations in ER-shaping proteins^{3,4}. Measurements of ER-luminal protein mobility using fluorescence recovery after photo-bleaching (FRAP) have previously uncovered an energy dependence that is difficult to reconcile with passive diffusion^{5,6}. An increase in luminal crowding due to the incapacitation of ATP-dependent ER chaperones has been suggested as a plausible explanation for this effect (direct crowding measurements here do not detect such an effect). Addressing this paradox remained challenging since FRAP measurements report on bulk mobility, and do not inform as to the nature of forces driving mobility at a molecular level. A passive diffusion model for luminal transport is also challenged by the notion that traversal time of random walking molecules increases exponentially with distance. This poses kinetic limits for material exchange in an expanded ER network. Recent advances in super-resolution microscopy afford a basis for development of a single particle tracking approach to provide a detailed description of molecular motion in the ER lumen, with potential to generate a wealth of information regarding directionality and velocity from a large number of simultaneous single-molecule displacement events. Using live cell super-resolution microscopy, we visualised and analysed single molecule trajectories traversing tubular ER, and the organelle's real-time morphological dynamics.

First we examined, in our experimental system, the energy dependence of luminal protein mobility, previously demonstrated for green fluorescent protein (GFP) using FRAP⁶. Escape-rate of photo-convertible fluorescent protein (Dendra2-ER) from a region of activation was attenuated by ATP depletion ([Fig. 1a](#)). This may reflect either an increase in resistance to motion or a decrease in active transport of proteins upon energy starvation. The former is contradicted by measurements of ER crowdedness, using a sensitive FRET-based probe⁷, that, over a broad range of expression levels, remained unaltered by ATP-depletion (Fig. 1b – d, [Supplementary Fig. 1a](#)). Furthermore, displacement of Dendra2 proteins (initially localized as a “packet” in a small volume of the tubular ER that had been subjected to a colour-photoswitching laser pulse) occurred with variable speed and had a conspicuous unidirectional component ([Fig. 1e, Supplementary Video1](#)). These features are inconsistent with Brownian motion and suggest, instead, active transport.

To characterize motion in the ER lumen we performed real-time single particle tracking (SPT) in live cells, acquiring trajectories at optical super-resolution. Imaging at 56 Hz, we recorded single molecule fluorescent signals from functional (Halo-tagged ER luminal chaperone, Calreticulin, Crt) and inert (ER targeted HaloTag) proteins, both sparsely labelled with a fluorescent ligand (chloroalkane-Tetramethylrhodamine, TMR). Brightness and photostability of the TMR ligand enabled tracking single particles over longer trajectories than genetically-encoded fluorophores ([Supplementary Fig. 1b](#)), thus establishing spatio-temporal correlations in motion patterns over extended periods of time. This approach offered information on directionality and instantaneous velocity at a single molecule level, not available in bulk methods such as FRAP. By implementing a single molecule localisation algorithm, images reconstructed from the SPT series revealed a pattern typical of the ER network, confirming ER-localisation of the HaloTag-Crt and washout of the unbound dye ([Fig. 2a & b, Supplementary Videos 2–4](#)).

Trajectories were generated from single-molecule time series by sequentially implementing spot detection and tracking algorithms^{8,9}. ER geometry constrains particle movement to a narrow tubular network, which limits overlapping trajectories, contributing to the tracking algorithm's ability to faithfully trace many molecules simultaneously. Resulting trajectories reconstruct a map recognizable as a pattern of ER tubes and their connecting reservoirs (Fig. 2c), reflecting tracking fidelity. Notably, spatio-temporal particle distributions were non-uniform, with higher time-integrated abundance in the tube-connecting reservoirs (Fig. 2d). This heterogeneity correlated with spatial distribution of instantaneous velocities, revealing distinct subgroups: relatively slow-moving particles predominantly detectable in segments of trajectories mapped to the nodes and particles with relatively high and variable velocities mapped to node-connecting tubes (Fig. 2c). These characteristics could be observed for two different markers (Calreticulin and HaloTagER) and three different cell types (HEK 293T, COS-7, SH-SY5Y, Supplementary Table 1). The long, single-tailed velocity distribution observed (histogram, Fig. 2c) is incompatible with Brownian motion (Fig. 2c, modelled by solid line). Furthermore, ATP depletion led to selective loss of the fast-moving population (Fig. 2e). These observations suggest that diffusive motion is manifest by the slow-moving particles in the tube-connecting reservoirs (nodes), while the rapidly-moving particles in the tubes are subjected to an ATP-dependent propulsive force, resulting in an ER luminal flow. The displacement profile observed fits well a bi-modal distribution of instantaneous velocities (Fig. 2c, modelled by dashed line).

Next we quantified temporal coordinate changes of HaloTag-Crt by analysing SPT data using the overdamped limit of the Langevin model (where velocity is described as the sum of diffusional and drift forces, and motion parameters are estimated from local statistics of the displacement, see Methods)¹⁰⁻¹³. Motion is described by the stochastic model (a sum of directed

and diffusional motion terms): $\dot{X} = b(X) + \sqrt{2D(X)} \dot{w}$, (1) where w is Brownian motion. The source of the noise w is the ambient thermal agitation, while the drift term b represents transport in tubules and D is the effective local diffusion. This analysis (see [Supplementary Note 1](#)) allows estimating D and b from large numbers ($\sim 10^4$ per cell acquisition) of single particle trajectories.

The global nature of this statistical approach considers not only particle displacement speed but also direction patterns, extracted from a large number of trajectories repeatedly traversing the same regions, thereby unmixing the contribution of Brownian and deterministic forces. This computation identifies a slow diffusional ($D=0.19\pm0.13 \text{ }\mu\text{m/s}^2$) component that maps predominantly onto the nodes ([Fig. 2f](#)). The relatively fast movement of internode particles required an additional component to account for their directionality and persistence, consistent with a propulsive force with normal distribution of velocity ($22.9\pm6.92 \text{ }\mu\text{m/s}$, [Fig. 2g](#)). The super-diffusive nature of particle motion in ER tubules was further confirmed by analysis of time-averaged mean squared displacement (MSD) of SPT. MSD described as $\sim t^\alpha$, where the anomalous exponent α defines motion as sub-diffusive if $\alpha<1$, Brownian/diffusive if $\alpha=1$ and super-diffusive if $\alpha>1$. Conducted on the entire ensemble of trajectories, the MSD analysis revealed a broad range of particle behaviours ($0<\alpha<1.5$, [Fig. 2b](#)), whereas the same analysis restricted to trajectory fragments located in nodes revealed clearly confined diffusion dynamics ($\alpha<0.8$, [Supplementary Fig. 2c](#)). Trajectories of particles moving outside the nodes exhibited super-diffusive dynamics ($\alpha>1$, [Supplementary Fig. 2d, Video 3](#)). These results are consistent with the active motion mode identified in analysis of Figure 2.

Similar observations were made in Green Monkey kidney (COS-7) and Human neuroblastoma (SH-SY5Y) cell lines, attesting to their broad validity in describing ER flow dynamics and its spatial organization ([Supplementary Fig. 3, Table1, Video 2](#)). Measurements of

the motion parameters of a lower mass ER-localised protein, HaloTag-KDEL, showed similar values to those observed with the tagged Crt ([Supplementary Fig. 3, Table1](#)). Flow velocity was slightly higher in COS cells than in HEK-293T and SH-SY5Y cells. The behaviour of the luminal ER markers, HaloTag-KDEL and Calreticulin, contrasted with that of a membrane-associated analogue of the latter, mEOS2-Calnexin: its velocities were distributed relatively homogeneously through the ER network (Fig. 3a, b), lacked the thick tail of high values in distribution of instantaneous velocities and fit well to a purely diffusional model ([Fig. 3a-d](#)).

To establish whether recently reported ER macrostructure motion characteristics¹⁴ are reflected in the SPT analysis, we focused on their numerical parameters. Motion of ER tubules characterized by their relatively slow transverse oscillation (4Hz, with an amplitude < 50 nm, which translates to velocity <0.2 $\mu\text{m}/\text{s}$ ¹⁴), does not significantly contribute to the relatively fast velocities of flow-assisted marker particles moving along the tubules (27-42 $\mu\text{m}/\text{s}$, [Supplementary Table 1](#)). Junction fluctuations contribute a similarly insignificant component to the diffusional motion inside the junction since the diffusion coefficient calculated from tracking of whole junctions was 69 times slower than the mean diffusion coefficient computed for single molecules (¹⁴, [Supplementary Fig. 4, and Video 5](#)). Furthermore, contribution of tubule growth to single particle trajectories was found to be negligible, with a mean percentage of tubules growing at any given time of 0.14 +/- 0.04 % ([Supplementary Videos 5-7](#)).

Consistently, considering trajectory motion as a purely diffusive process yielded an apparent diffusion coefficient of 1.13 $\mu\text{m}^2/\text{s}$ ([Fig. S2a](#)) similar to that previously estimated by FRAP^{5, 15, 16}.

Though most individual trajectories visited only a limited number of nodes ([Fig. 4a](#)), an Oriented Network Graph analysis, which identifies directly or proxy interconnected junctions

through trajectory directions¹⁷ revealed that, regardless of their starting point, particles have the potential to visit almost the entire ER network (Fig. 4b; the disconnected periphery is likely contributed by signals from neighbouring cell(s)). This analysis is consistent with the notion that the ER network maintains a luminal continuum. The ER appeared to be in a state of equilibrium, with nodes, on average, connected by an equal number of inward and outward trajectories (Fig. 4c & d). These findings are consistent with an interconnected system of flows that preserves the content across the ER.

Closer scrutiny of the directionality of individual tube-traversing particles suggested a pattern whereby the direction of visible flow alternates with variable frequency (switching on average every 4 seconds, maintained for up to 14 seconds Fig. 5a & b); and particles accelerated periodically following their exit from a node, reaching brief velocity peaks that lasted up to 120 ms (Fig. 5c & d). Intervals between velocity peaks and flow-directionality alternations were distributed stochastically (Fig. 5b, d), suggesting that flow-inducing events (e.g. transient tubule contractions, discussed below) are not produced by synchronized oscillators and are therefore not centrally coordinated. However, we cannot exclude the contribution of synchronization processes whose phase is lost, as trajectories are recorded asynchronously. Note that temporal profiles of directionality are not available using low spatio-temporal resolution approaches (e.g. FRAP or photoconversion pulse-chase, Fig. 1e).

The oscillatory luminal motion suggested the possibility of nanoperistalsis-like¹⁸ propulsion, attainable by tubule contractions. To test this, we obtained high-resolution time-series images of the ER tube structure of live cells by fast Structured Illumination Microscopy (SIM)^{14,19,20}. These revealed transient, asynchronous constriction of the tubes at specific locations (Fig. 5e, Supplementary Fig. 5a, b; Video8 & 9), consistent with a role for tube constriction in generating

flow. Constriction-driven propulsion is also consistent with the observed velocity values and variation of packets of photo-converted Dendra2 during their deterministic traversal of the tubular ER ($V_{max} = 19.9 \mu\text{m/s}$, Fig. 1e). Furthermore, frequency of contraction events decreased four-fold upon ATP depletion (Fig. 5f, Supplementary Video 10). It is expected that following an individual contraction event (with a frequency of hundreds of milliseconds), both deterministic and acceleratory displacement of multiple particles would be detected, as SPT acquisition operates at approximately ten times the contraction frequency. Assuming uncoordinated contractions throughout the tubular network, consecutive contractions have the same probability to preserve or invert the direction of the next set of detectable SPT events (consistent with observed distribution of directionality preservation time, Fig. 5b).

The notion that tubule contractions generate high-velocity peaks in luminal particles is supported by the fact that their temporal distributions are both Poissonian (Fig. 5d & g), indicating compatible physical processes. The larger time constant of contractions (~900ms) compared to that of high-velocity peaks (~80ms) is expected since several contraction points may contribute to the particles' acceleration incidence.

Furthermore, a physical model simulating forces resulting from tubule contraction, and based on their empirical characteristics (Fig. 5h and Supplementary Note1), predicts flow velocities of 10-40 $\mu\text{m/s}$, in agreement with the high-velocities observed in SPT (Fig. 5c). Notably, the contraction frequency is low enough to avoid coinciding proximal contractions that may cancel the local flows (probability of simultaneous contractions of two points = 0.022, calculations in Supplementary Note 1). Whilst the existence of a mechanism for spatio-temporal coordination of the contraction events cannot be ruled out, our findings indicate that an uncoordinated system, inducing fast local currents with alternating directionality inside the tubular network, is sufficient

to ensure a rapid luminal content homogenization/distribution and thereby overcome a critical kinetic limitation of passive diffusion as a mechanism for ER content mixing in large cells.

Localised contraction of ER tubules, leading to ER deformation, was observed during calcium manipulation²¹ ([Supplementary Fig. 5c](#)), or phototoxicity ([Supplementary Fig. 5e](#) and [Video 11](#)), both reversible processes affecting ER morphology ([Supplementary Fig. 5e](#)). These super-resolved images of the ER's structural dynamics under severe experimental perturbation highlight a potential for ER tubes to contract, revealing that fragments of the perturbed ER that had lost their tubular structure displayed characteristically slow-velocity diffusional motion ([Supplementary Fig. 5d](#)). Other physiological membrane dynamic processes involving molecular motors, vesicular fusion and budding, network oscillation¹⁴ and even tube elongation/withdrawal may also contribute to flow and warrant further investigation.

Regardless of its origin(s), the alternating luminal currents described here are well suited to serve as a mixing device, enhancing distribution of ER content throughout the cell. Given that diffusion-driven connectivity (matter exchange rate) decreases exponentially with distance, it is expected that the active process described here would be especially important in cells with extensive ER projections, such as motor neurones. It is therefore tempting to speculate that perturbed luminal flow might contribute to diseases such as hereditary spastic paraplegia, associated with defective ER membrane-shaping proteins^{3,4,22}.

Acknowledgements:

We are grateful to Matthew Gratian and Mark Bowen (CIMR, Cambridge) and Gregory Strachan (Institute of Metabolic Science, Cambridge) for assistance in establishing microscopy data acquisition approaches; Steffen Preissler (CIMR, Cambridge) for discussion.

This study was supported by grants from Wellcome Trust to DR (Wellcome 200848/Z/16/Z, WT: UNS18966); Wellcome Trust Strategic Award for core facilities to the Cambridge Institute for Medical Research (Wellcome 100140); EPSRC (EP/L015889/1 and EP/H018301/1), MRC (MR/K015850/1 and MR/K02292X/1) and Wellcome Trust (3-3249/Z/16/Z and 089703/Z/09/Z) to CFK; FRM team research grant to DH; a DIM fellowship from Ile-de-France to PP. DR is a Wellcome Trust Principal Research Fellow. EA is a United Kingdom Dementia Research Institute Fellow.

Figure Legends:**Fig. 1. ATP depletion affects ER mobility without altering luminal crowdedness.**

- (a) Trace of time-dependent decay in the intensity of the fluorescence signal from an ER-localised photoconvertible protein, Dendra2-ER, after a pulse of photo-converting illumination delivered to a small patch of untreated or ATP-depleted COS7 cells. Inset denotes mean \pm SEM, (n=5 traces per condition) of fluorescence decay half time, reflecting the probe's escape from the photoconversion area.
- (b) Fluorescence intensity (left) and colour-coded fluorescence lifetime (FLT) images (right) of COS7 cells transfected with an ER-localised molecular crowding probe⁷. FLT distribution within imaged cells is displayed in colour-coded histograms with mean FLT noted (in picoseconds, ps, right). Cells were left untreated (UNT), ATP depleted, or treated with hyper-osmotic (Hyper Os.) or hypo-osmotic buffers that induce cell shrinking or swelling to obtain maximal and minimal crowding values, respectively. Shown are characteristic images observed in three independent repeats.
- (c) Bar diagram of FRET-donor FLT values measured as in (b) (mean values \pm SD, n=22 independently sampled cells).
- (d) Bar diagram of relative intracellular ATP concentration measured with FRET-based ATP-probe (A-Team)²³ in cells untreated or ATP depleted as in (a & b). Minimum and maximum values represent the probe readings in ATP depleted or saturating conditions respectively, imposed in semi-permeabilised cells. Shown are mean values \pm SD, n=10 independently sampled cells.
- (e) Images of COS7 cell expressing Dendra2. A brief pulse of illumination photoconverted

Dendra2 from green to red in a restricted region of the ER. The progression of the photoconverted packet of proteins is revealed by the time series and summated in the bottom panel with its velocity colour coded.

Fig. 2. Characteristics of single particle displacement tracked in the tubular ER lumen.

- (a) Image reconstructed from single molecule localizations of TMR-labeled Halo-tagged Calreticulin (Crt), in HEK-293 cells, rendered with a molecular density colour code.
- (b) Skeletonization view of image in (a). Shown are representatives of n=3 independent experiments.
- (c) Single molecule trajectories generated using particle-tracking algorithm from time series of image (a)), color-coded according to instantaneous velocity distribution shown in histogram. Overlaid traces: velocity distribution simulated assuming exclusively diffusion-driven motion (solid line, using apparent D from (f)), or combination of diffusion and flow (using D and flow rate from f & g). Inset: cumulative distribution, Kolmogorov-Smirnov test of observed vs. expected distributions.
- (d) Density map computed for grid of square bins (sides of 0.2 μm) imposed on particle displacement map. Ellipses mark boundaries of higher density regions (correspond to tube-connecting reservoirs/junctions).
- (e) Histograms of instantaneous velocity frequency distributions of SPT from a cell before/after ATP depletion (as in Fig. 1 a-c). Inset: violin plot presenting the medians (red bars) and density (grey) of the distributions. A two-sided Mann-Whitney U-test was used to compare median of each pair of distributions (** p-value < 1e-3), $p_{(0-20 \text{ min})}=1\text{e-}80$, $p_{(20-40 \text{ min})}=9.889\text{e-}64$, $p_{(0-40 \text{ min})}=1\text{e-}80$; n=20526, n=14591 and n=10108 trajectory displacements respectively.
- (f) Diffusion map extracted from the empirical estimator of the Langevin equation (1) and computed from a square grid as in d. Inset: distributions of the diffusion coefficients inside nodes

(AVG +/- SD=0.19 +/- 0.13, n=226 nodes).

(g) Flow map computed by averaging non-Brownian velocity jumps of particles moving between pairs of neighbouring nodes identified in (d) and color-coded according to the inset histogram. Inset: distribution of average instantaneous velocity between pairs of neighbouring nodes (n=705 node-pairs; AVG +/- SD=22.90 +/- 6.92).

Raw source single molecule time series and image-reconstruction are shown in [Supplementary Video 2](#).

Fig. 3. Statistics of Single Particle trajectories recorded from the ER membrane.

- (a) Single molecule trajectories of mEOS2-calnexin expressed in HEK-293 cells generated as in Figure 2, color-coded according to instantaneous velocity distribution Inset: Instantaneous velocity distribution histograms computed from the displacements extracted from the trajectories and overlaid by the expected distribution for a purely diffusive motion with the diffusion coefficient extracted from (d).
- (b) Density map computed for a grid of square bins (sides of 0.4 μm) imposed on the particle displacement map.
- (c) Diffusion map extracted from the empirical estimator of the Langevin equation (1, methods) and computed from the same square grid as in (b).
- (d) Histograms of diffusion coefficients computed from individual square bins, pooled from two cells, for the entire domain as presented in (c). The red curve on top of the diffusion histogram corresponds to a fit (Trust Region Reflecting algorithm) to a Gaussian distribution with $\mu_D = 0.42 \mu\text{m}^2/\text{s}$, $\sigma_D = 0.12 \mu\text{m}^2/\text{s}$ and a determination coefficient $R^2 = 0.986$. Descriptive statistics given as AVG +/- SD.

Fig. 4 Properties of ER luminal trajectories' directionality.

(a) Number of nodes visited by individual particles. Trajectories map, as in [Figure 2](#), colour-coded according to the number of nodes visited by a particle; and the distribution of the number of nodes visited by each individual trajectory (excluding trajectories visiting 0 node).

(b) Vectorial representation of the ER network from [Figure 2](#) analysed using Oriented Network Graph analysis, to assess the direct or proxy, uni/bi-lateral trajectory-connectivity of the nodes, assigning single colour for each interconnected area. Note a strong connected component resulting in a monochromatic appearance of almost the entire network. Arrows denote prevalent displacement directionality (detected in 18% of tubes), defined as such if steady-state ratio of flow in one direction vs. the total flow exceed 0.75. Dashed links represent flows whose directionality could not be determined due to insufficient number of displacement events.

(c) Distribution histogram of the number of outward (efferent) and inward (afferent) directed branching for individual nodes. Efferent branches were defined as the number of nodes, reached by the outward trajectories originating in the examined node, in the time-integrated map; accordingly, afferent branches reflect the number of nodes-of-origin for the trajectories arriving at the examined node.

(d) Distribution of the fraction of exiting trajectories for each node.

All values are given as AVG \pm SD.

Fig. 5. Dynamics of ER luminal flow correlated with tubule contractions.

- a. Analysis of particle trajectories' directionality. Tubular junctions/nodes denoted by orange ellipses; grey lines denote all particle trajectories. Trajectories connecting two nodes indicated as A and B are colour coded according to their direction either in blue, denoting travel from A to B, or red for travel from B to A. Lower graph represents the temporal pattern of traversal-directionality. Shown is representative of n=108 node-pairs.
- b. Distribution of time periods of unidirectional inter-node displacement.
- c. Plots of instantaneous particle velocities fluctuations. Velocities of particles following departure from nodes and traveling along tubules (between nodes, red), and those of particles residing within nodes (black). Solid lines represent mean values for all trajectories, shaded regions represent SD of total sample size: n=111 internode and n=140 intranode trajectory displacements.
- d. Analysis of time duration T_H of high-velocity ($v > 20 \mu\text{m}/\text{s}$) peaks (left) and time interval T_L between high-velocity peaks. Red line represents an exponential fit ($R^2 = 0.998$).
- e. High-speed Structured Illumination Microscopy (SIM) super-resolved images of the tubular ER in live COS7 cells stained with an ER membrane dye (ER Tracker-Green). Images were acquired in 54 ms intervals and processed as described in Methods. The resulting SIM reconstructions were colour-coded according to intensity. The magnified area shows the contours of ER tubules at higher magnification. Arrows denote positions where transient contraction events occur repeatedly. Shown are frames from a time series measurement presented in full in supplementary

Video S8. Tubule contractions are better visualized in COS7 cells, but detectable in HEK-293 cells too (Fig. S5). Shown is representative of n=5 independent experiments.

f. Box plot of tubule contraction frequencies extracted from high-speed SIM time series as shown in (e) before and after ATP depletion. Red line – median, boxes' bottom/top edges – the 25th and 75th percentiles respectively, whiskers – extreme data points. ***: Two-sided Mann-Whitney U-test p=1.7019e-7, n=20 ER tubules.

g. Distributions of contraction duration, intervals and lengths from SIM videos as in (e) and Fig. S5. Red curves: exponential (left and middle) and Gaussian (right) fits ($R^2 = 0.988$, $R^2 = 0.969$, $R^2 = 0.937$ respectively).

h. Schematic representation of the model for estimating tubule contraction-induced particle velocity.

All values are given as AVG \pm SD for noted n.

References:

1. Powers, R.E., Wang, S., Liu, T.Y. & Rapoport, T.A. Reconstitution of the tubular endoplasmic reticulum network with purified components. *Nature* **543**, 257-260 (2017).
2. Voeltz, G.K., Prinz, W.A., Shibata, Y., Rist, J.M. & Rapoport, T.A. A class of membrane proteins shaping the tubular endoplasmic reticulum. *Cell* **124**, 573-586 (2006).
3. Hubner, C.A. & Kurth, I. Membrane-shaping disorders: a common pathway in axon degeneration. *Brain : a journal of neurology* **137**, 3109-3121 (2014).
4. Blackstone, C., O'Kane, C.J. & Reid, E. Hereditary spastic paraplegias: membrane traffic and the motor pathway. *Nature reviews. Neuroscience* **12**, 31-42 (2011).
5. Dayel, M.J., Hom, E.F. & Verkman, A.S. Diffusion of green fluorescent protein in the aqueous-phase lumen of endoplasmic reticulum. *Biophysical journal* **76**, 2843-2851 (1999).
6. Nehls, S. *et al.* Dynamics and retention of misfolded proteins in native ER membranes. *Nature cell biology* **2**, 288-295 (2000).
7. Boersma, A.J., Zuhorn, I.S. & Poolman, B. A sensor for quantification of macromolecular crowding in living cells. *Nature methods* **12**, 227-229, 221 p following 229 (2015).
8. Cheezum, M.K., Walker, W.F. & Guilford, W.H. Quantitative comparison of algorithms for tracking single fluorescent particles. *Biophysical journal* **81**, 2378-2388 (2001).
9. Chenouard, N. *et al.* Objective comparison of particle tracking methods. *Nature methods* **11**, 281-289 (2014).
10. Schuss, Z. Theory and Applications of Stochastic Processes. *Appl Math Sci* **170**, Cover1-U4 (2010).
11. Hoze, N. & Holcman, D. Residence times of receptors in dendritic spines analyzed by stochastic simulations in empirical domains. *Biophysical journal* **107**, 3008-3017 (2014).
12. Hoze, N. *et al.* Heterogeneity of AMPA receptor trafficking and molecular interactions revealed by superresolution analysis of live cell imaging. *Proceedings of the National Academy of Sciences of the United States of America* **109**, 17052-17057 (2012).
13. Langevin, P. The theory of brownian movement. *Cr Hebd Acad Sci* **146**, 530-533 (1908).
14. Nixon-Abell, J. *et al.* Increased spatiotemporal resolution reveals highly dynamic dense tubular matrices in the peripheral ER. *Science* **354** (2016).
15. Lai, C.W., Aronson, D.E. & Snapp, E.L. BiP availability distinguishes states of homeostasis and stress in the endoplasmic reticulum of living cells. *Molecular biology of the cell* **21**, 1909-1921 (2010).
16. Snapp, E.L., Sharma, A., Lippincott-Schwartz, J. & Hegde, R.S. Monitoring chaperone engagement of substrates in the endoplasmic reticulum of live cells. *Proceedings of the National Academy of Sciences of the United States of America* **103**, 6536-6541 (2006).
17. Tarjan, R. Depth first search and linear graph algorithms. *Siam Journal on Computing* **1** (1972).
18. Nadeem, S. & Maraj, E.N. The mathematical analysis for peristaltic flow of nano fluid in a curved channel with compliant walls. *Applied Nanoscience* **4**, 85-92 (2014).
19. Young, L.J., Strohl, F. & Kaminski, C.F. A Guide to Structured Illumination TIRF Microscopy at High Speed with Multiple Colors. *Journal of visualized experiments : JoVE* (2016).
20. Kner, P., Chhun, B.B., Griffis, E.R., Winoto, L. & Gustafsson, M.G. Super-resolution video microscopy of live cells by structured illumination. *Nature methods* **6**, 339-342 (2009).
21. Subramanian, K. & Meyer, T. Calcium-induced restructuring of nuclear envelope and endoplasmic reticulum calcium stores. *Cell* **89**, 963-971 (1997).
22. Lo Giudice, T., Lombardi, F., Santorelli, F.M., Kawarai, T. & Orlacchio, A. Hereditary spastic paraplegia: clinical-genetic characteristics and evolving molecular mechanisms. *Experimental neurology* **261**, 518-539 (2014).
23. Imamura, H. *et al.* Visualization of ATP levels inside single living cells with fluorescence resonance energy transfer-based genetically encoded indicators. *Proceedings of the National Academy of Sciences of the United States of America* **106**, 15651-15656 (2009).
24. Gustafsson, M.G. *et al.* Three-dimensional resolution doubling in wide-field fluorescence microscopy by structured illumination. *Biophysical journal* **94**, 4957-4970 (2008).

Methods

1 Intra-vital and fixation cell microscopy

1.1 Cell culture, transfections and expression constructs

COS7 (RRID:CVCL_0224), HEK 293 cells were cultured in Dulbecco's Modified Eagle's medium (DMEM) supplemented with 10% foetal calf serum and 1X non-essential amino acids (M7145 -SIGMA, Gillingham, Dorset, UK). SHSY-5Y cells were cultured in MEM/F12 medium supplemented with 15% foetal calf serum. Transfections were performed using the Neon Transfection System (Invitrogen, Paisley, UK) applying 1.5g of ATeam or crowding probe DNA to 3.10^5 cells. An expression vector encoding a cytosol localised crowding probe⁷ was modified to encode an endoplasmic reticulum localised probe by N-terminal addition of mouse pro

1.2 Photo-conversion microscopy

Photo-conversion pulse chase experiments were performed using Leica SP8 confocal microscope. Images were acquired using frame size of 256×256 pixels to allow imaging at 9 frames/sec rate, in Green (488 nm excitation, 510 - 530 nm emission) and Red (561 nm excitation, 590 - 620 nm emission) channels. Photo-conversion illumination (405 nm) was introduced at frame 20 in a region of interest for duration of 20 frames, using On The Fly FRAP acquisition mode (enabling image recording during the photoconverting illumination). Normalized intensity of the Red channel at the region of photo-conversion was plotted as a function of time post-photoconversion, and fitted to a mono-exponential decay function, to extract the decay $t_{1/2}$, that was used as an estimator of Dendra2-ER mobility.

1.3 Cell manipulations and Fluorescence Lifetime Imaging Microscopy (FLIM)

FLIM was carried out as previously described^{25,26}, using a pulsed (sub10ps, 20-40MHz) supercontinuum (430-2000nm) light source (SC 450, Fianium Ltd., Southampton, UK). An acousto-optic tunable filter (AA Optoelectronic AOTFnC-VIS) was used to define the 438 nm excitation wavelength for both the ER-crowding probe and ATeam ATP sensor. Emitted light was collected using a 470/20nm emission filter and detected by a fast photomultiplier tube (PMC-100, Becker & Hickl GmbH, Berlin, Germany). Data were processed using SPCImage (Becker & Hickl GmbH), fitting a monoexponential decay function. Osmosis-driven changes in cell volume were induced by addition of 0 mM NaCl (hypo-osmotic) or 500 mM NaCl (hyperosmotic) supplemented Hanks Balanced Salt solution (2.5mM KCl, 1.2 mM CaCl₂, 0.5

mM MgCl₂, 5 mM glucose, 10 mM HEPES pH 7.5) to a final ratio of 1:1 with DMEM (final osmolalities of 0.152 osmol/kg and 0.609 osmol/kg respectively). ATP depletion was achieved by incubating the cells in the presence of NaN₃ (0.05% w/v) and 2-deoxi-glucose (20 mM) for 2 hours prior to imaging; cells preserving the tubular ER pattern were selected upon treatments.

1.4 Single particle localisation and tracking (SPT)

Cells were transiently transfected with vectors encoding HaloTag (Promega) targeted to the ER by N-terminal the preprotrypsin signal sequence and a C-terminal retrieval signal (SS-HaloTag-KDEL); or Halo-Tag Calreticulin. 24 hours after transfection, cells were labelled with 0.5 nM cell-permeant HaloTag TMR ligand (tetra-methyl-rhodamine, Promega G8251) for 10 minutes, followed by 3 washes with label free medium; and imaged with 18 ms exposure on Elyra Super Resolution microscope (Zeiss) using α -Plan Apochromat X100 oil, 1.46C na objective; at 561/570-620 nm excitation/emission, in HiLo (pseudo-TIRF) mode using EMCCD iXON DU897 camera (Andor). The obtained single particle image series (at least 2000 frames) were processed using the PALM image reconstruction module or particle-tracking module at the instruments software (Elyra Zen edition, Zeiss). Trajectory generation fidelity was verified using the ICY software²⁷ version 1.9.5 and Imaris software version 8.4.1 (Bitplane).

The tracking algorithms was set to identify diffraction-limited spots as particles if their signal to noise ratio was > 4 and the spot does not exceed 9 pixels in diameter; then to identify the centers of spots to refine the positioning of the particle beyond the diffraction limit. The algorithm terminated trajectories if the signal disappears for 1 frame (linking is not permitted if particles leave the focal plane, blink etc.).

The tracking stage produces N_t two-dimensional trajectories $X_1 \dots X_{N_t}$ each possessing M_i points: $X_i(t_j) = [x_i^1(t_j), x_i^2(t_j)]$ ($1 \leq i \leq N_t, 0 \leq j < M_i$). Trajectories containing less than three points were discarded from the analysis. For each pair of successive points (t_{j+1}, t_j) of a trajectory i , we defined the displacement as: $\Delta X_i(t) = X_i(t_{j+1}) - X_i(t_j)$. See Supplementary Note 1 for further details of SPT mathematical analysis and modeling.

1.5 High-speed Structured Illumination microscopy

Live 2D-SIM (light modulation/grazing incidence illumination microscopy, GI-SIM) images of cells stained for 20 minutes with ER Tracker Green (ThermoFisher scientific, E34251) were acquired with a custom-built highspeed SIM microscope^{19,20}, using a spatial light modulator (SLM). ER Tracker Green was imaged using a 100X/1.49NA TIRF oil-immersion objective (Olympus) with a 488 nm diode laser (Toptica) at an irradiance of 50W/cm², with emission

imaged via a notch filter (FF01-525/30, Semrock) onto an sCMOS camera (ORCA Flash 4.0, Hamamatsu). 2D-SIM gratings displayed on the SLM resulted in a line spacing of 228 nm at the sample, corresponding to an angle of incidence of 44.6°. Each super-resolved frame was obtained from the reconstruction^{24,28} of nine raw frames acquired at 6 ms/exposure (54 ms/SIM frame). 3D-SIM (23 slices, 2.4 μm) was performed using Elyra microscope (Zeiss), with Plan Apochromat X63/1.4NA oil objective and sCMOS PCO Edge camera (Andor) on Paraformaldehyde 2%, Gluteraldehyde 2%, 100mM sodium cacodylate, 2mM CaCl₂, pH7.4 1 hour room temperature. See Supplementary Note 1 for further details of SIM image analysis.

Mathematical modelling and analysis

Details of the computational analyses of single particle tracking and structured illumination microscopy, and their mathematical modelling are described in Supplementary Note 1.

Statistics and Reproducibility

Statistical analyses and visualisation were performed using Matlab 9. Error bars, P values and statistical tests and sample sizes are reported in the figure legends. Statistical tests: differences between probability distribution were assessed using two-way Kolmogorov-Smirnov tests and differences between distribution medians were assessed using two-sided Mann-Whitney U-tests. All experiments were performed independently at least three times.

Code availability

Custom code generated for single particle tracking analysis and visualisation as well as for SIM ER network analysis of SIM images can be obtained from Zenodo database along with experimental raw data examples, DOI: 10.5281/zenodo.1317630 and DOI: 10.5281/zenodo.1318129 respectively.

Data Availability

Source image-series data for Fig. 1e, Supplementary Fig. 2 and Fig 4e, f have been provided as supplementary video1, 2 and 8 - 10 respectively; and statistical information for Fig. 2 and supplementary Fig. 2 have been provided in Supplementary Table 1. Custom code has been deposited in the Zenodo database DOI: 10.5281/zenodo.1317630 with experimental raw data DOI: 10.5281/zenodo.1318129. All other data supporting the findings of this study are available from the corresponding authors on reasonable request.

Figure 1

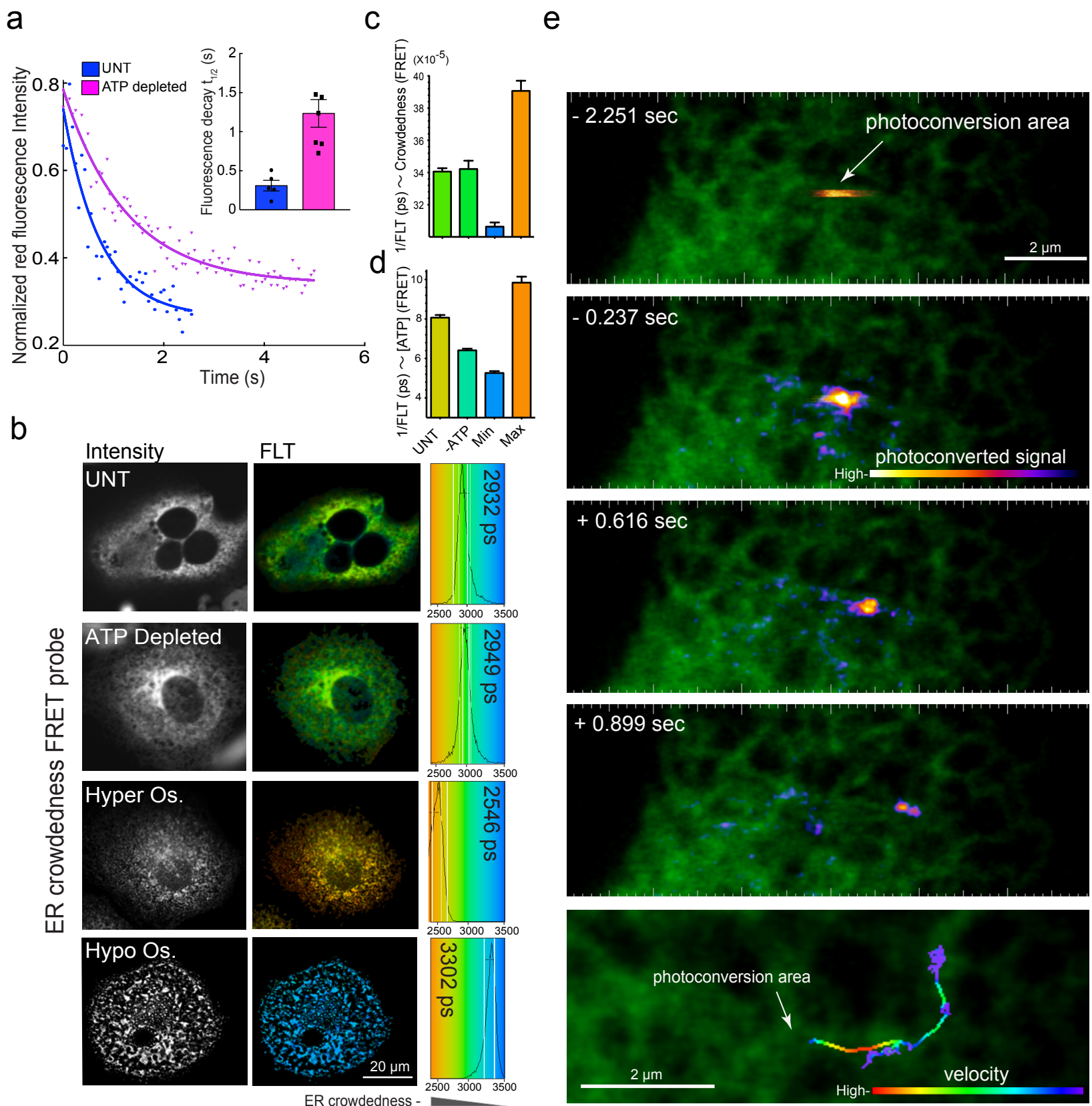


Figure 2

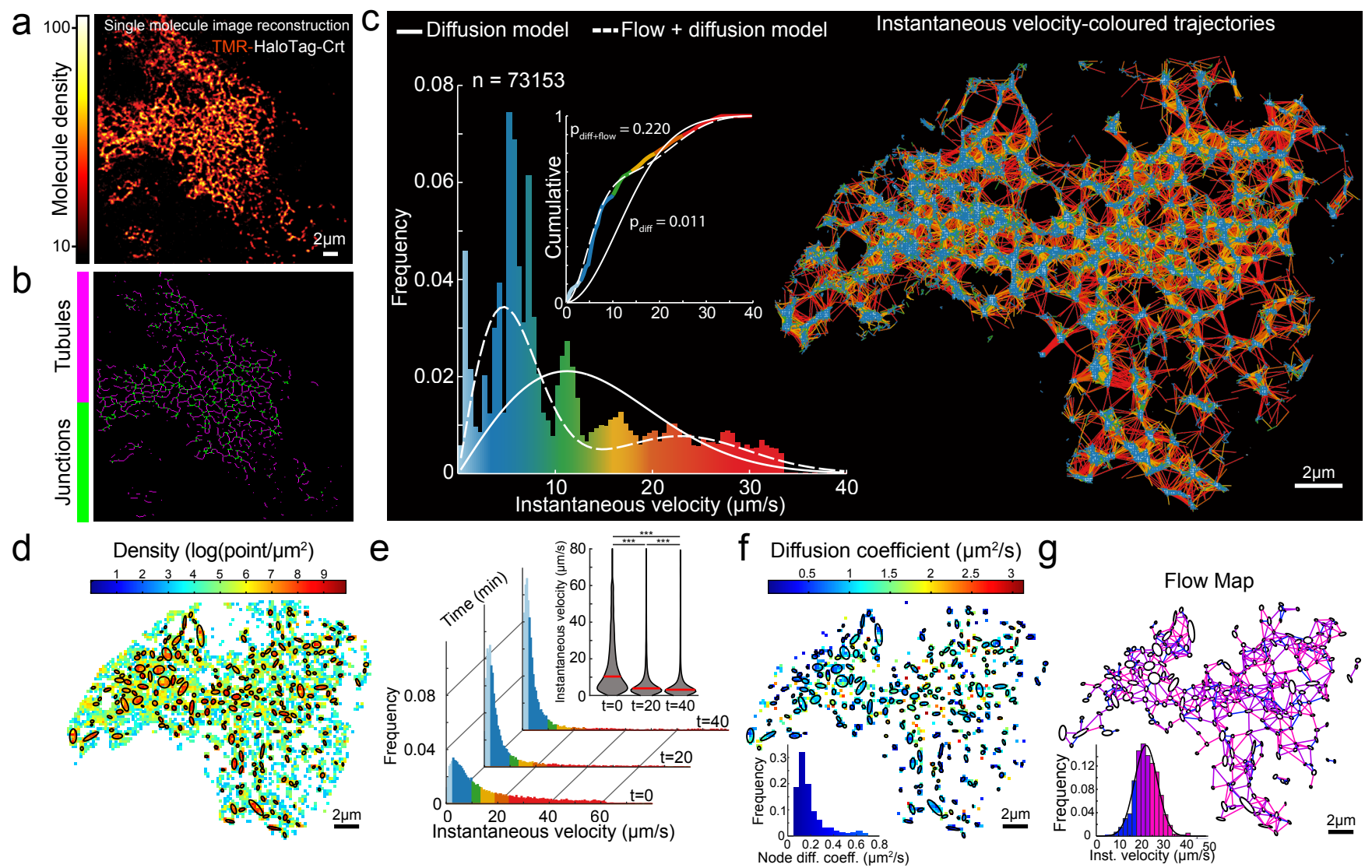


Figure 3

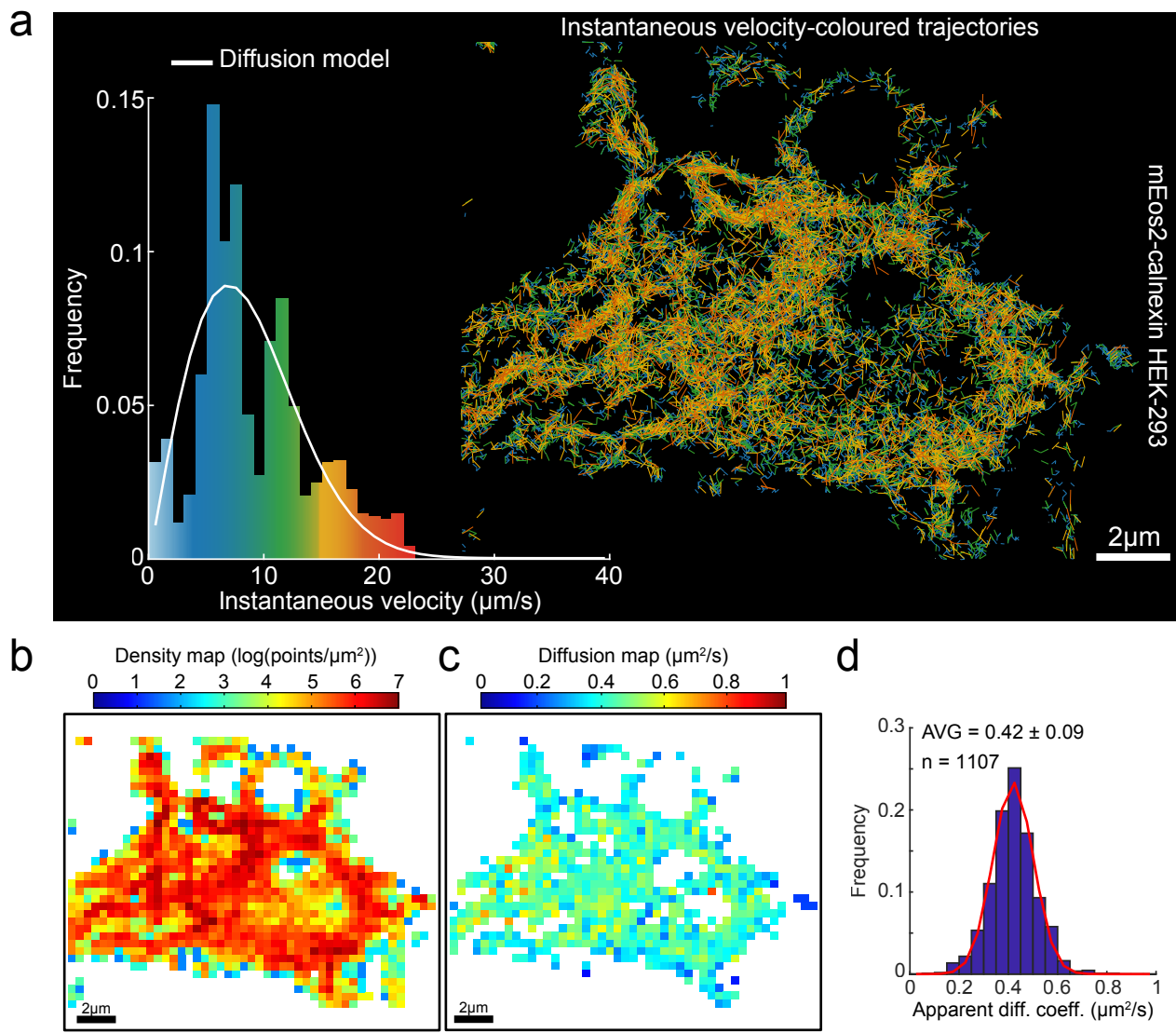


Figure 4

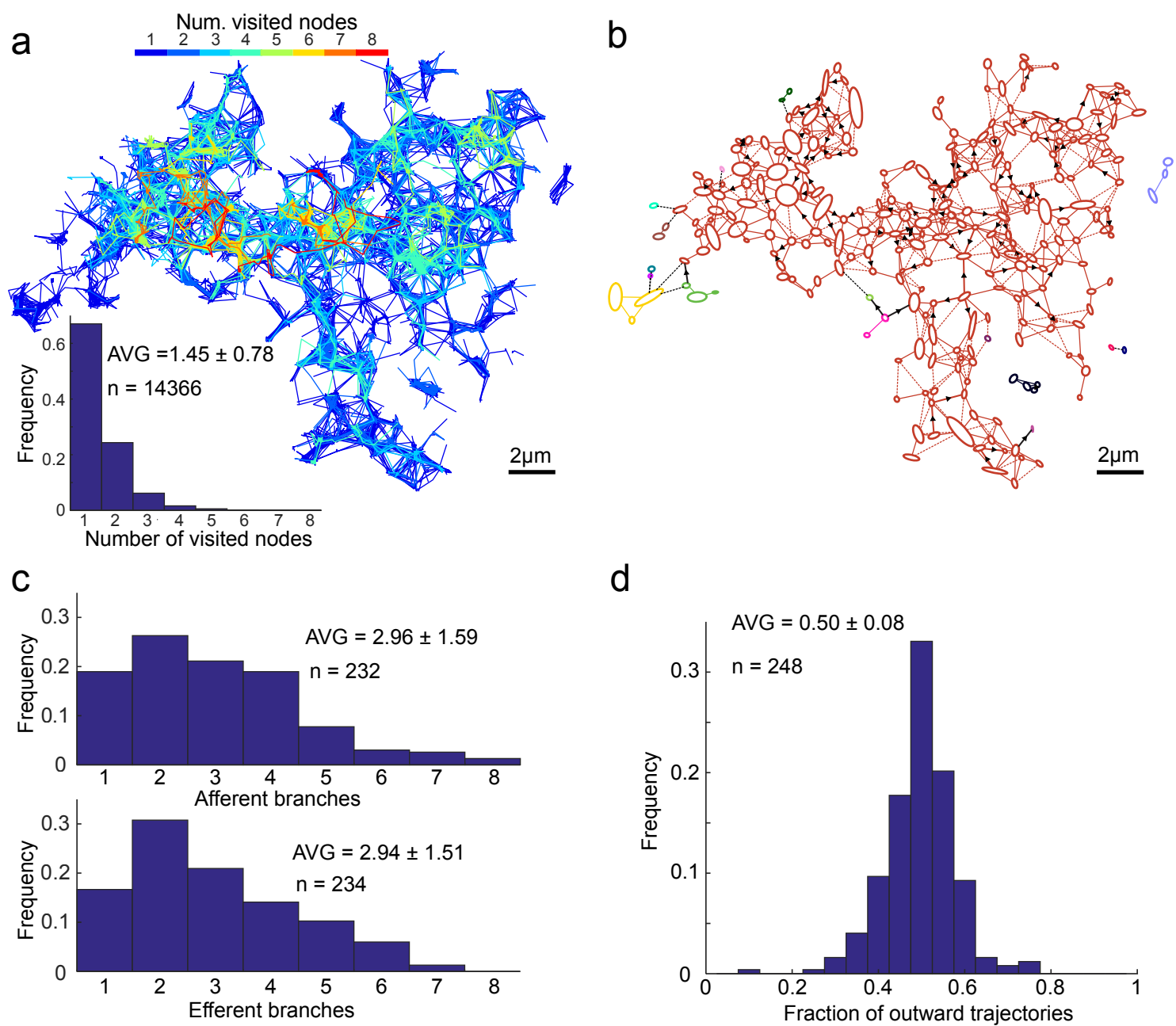
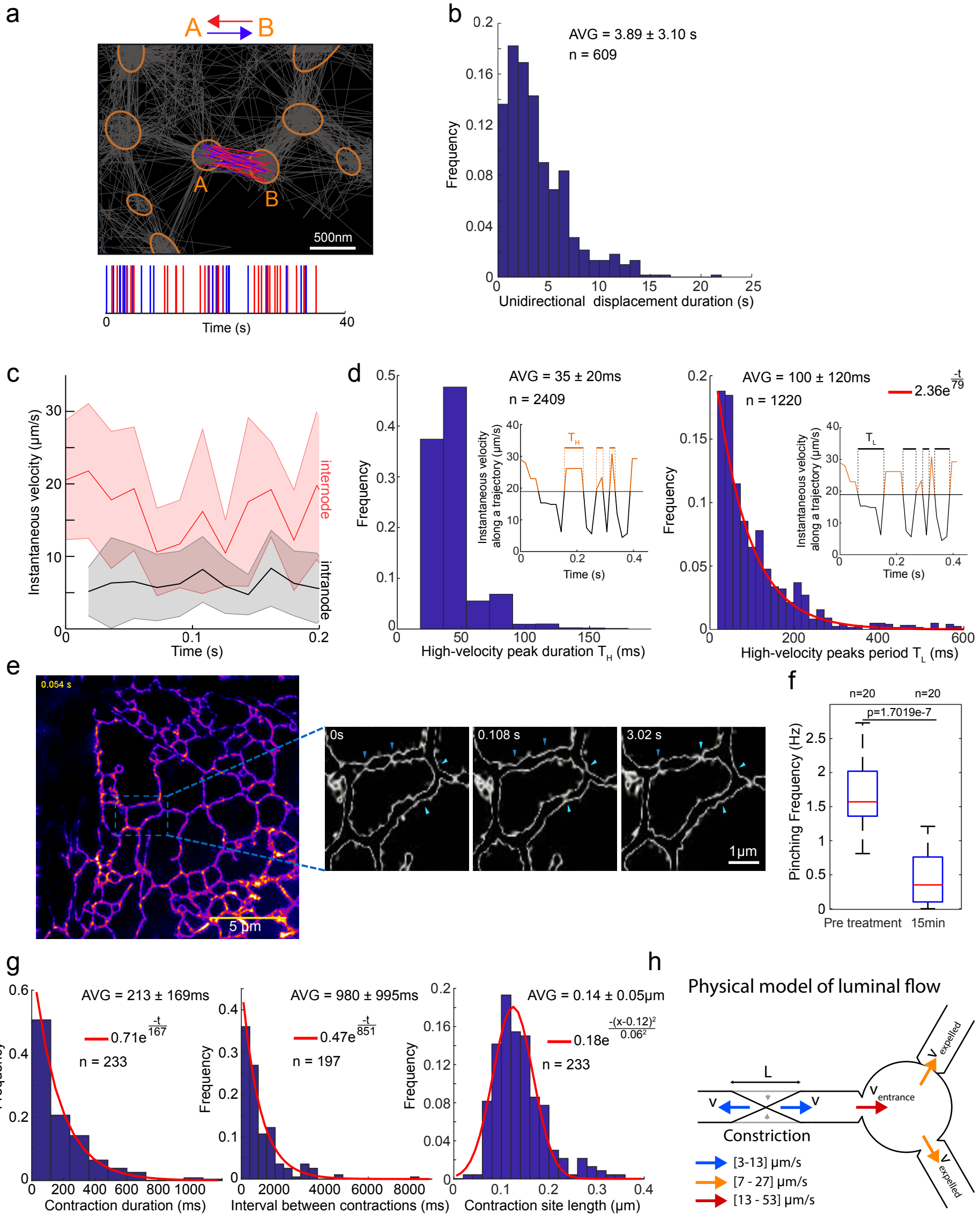
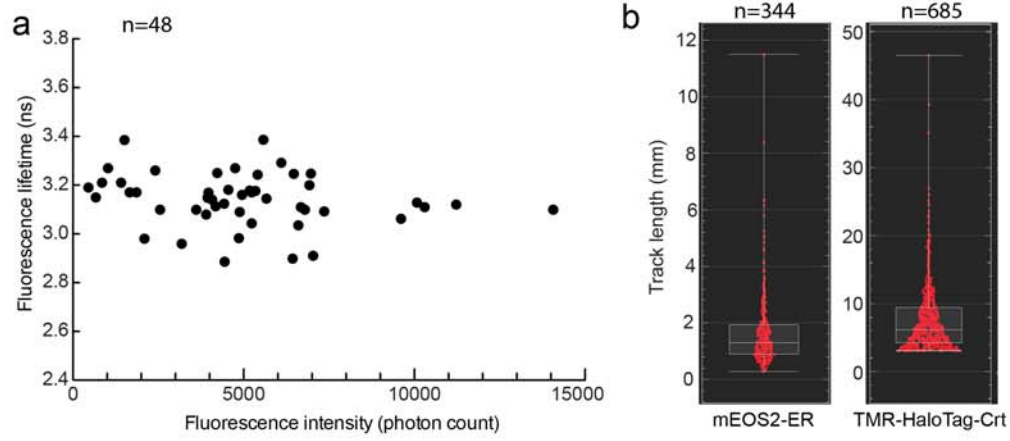


Figure 5

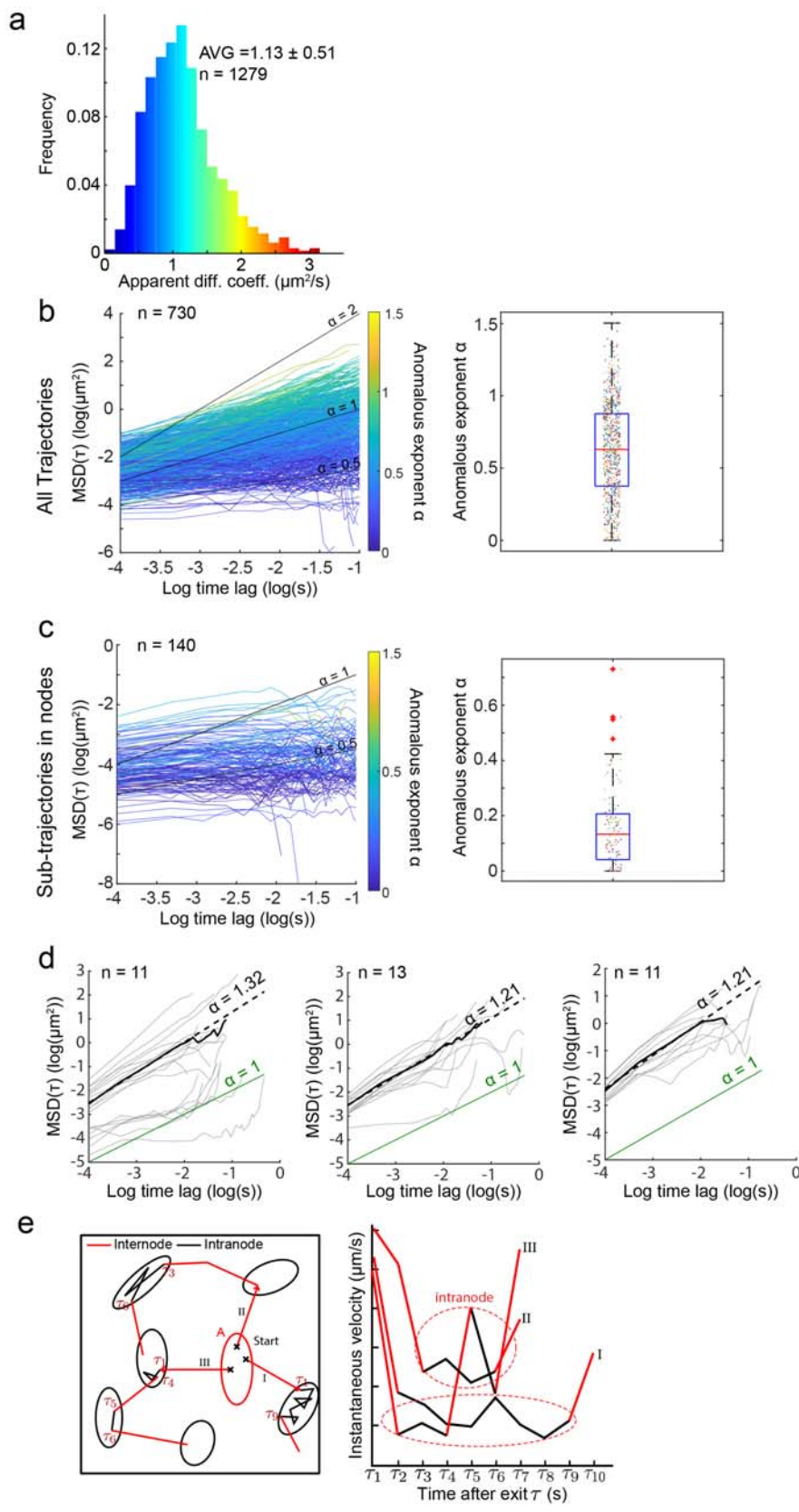




Supplementary Figure 1

Exogenous expression levels of a fluorescent protein do not affect macromolecular crowding in the ER lumen; TMR photostability affords longer SPT trajectories.

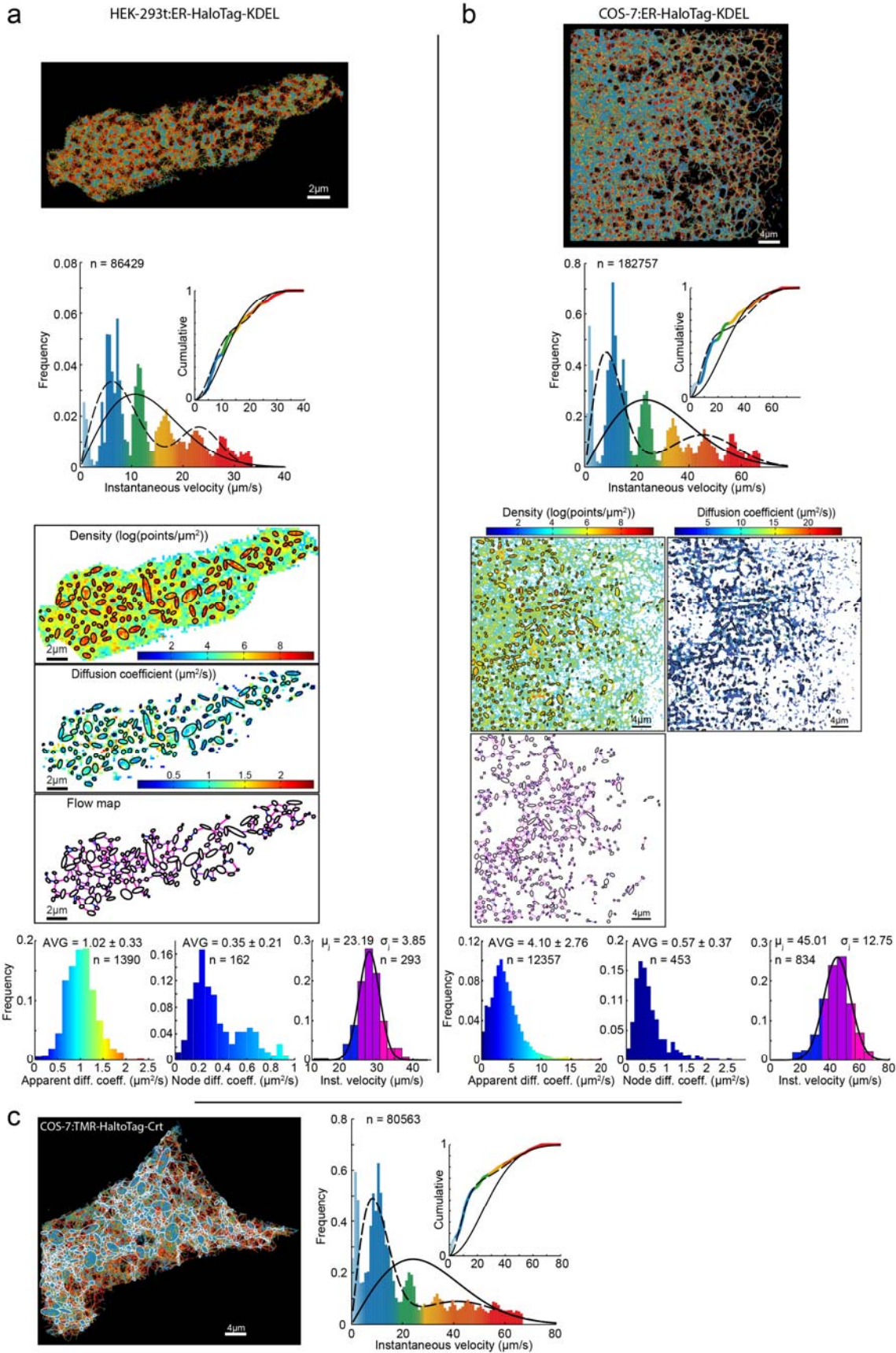
(a) Plot of fluorescence intensity versus fluorescence lifetime of individual cells expressing an ER-localised FRET-based macromolecular crowding probe as in Fig.1b. Fluorescence intensity serves as a measure of exogenous protein expression levels. Fluorescence lifetime correlates inversely with macromolecular crowding as described in Fig.1b. Note, no correlation (Pearson correlation coefficient $p=-0.2109$) was observed between the broad range of exogenous protein expression levels and macromolecular crowding, $n=48$ independently sampled cells (b) Distribution of trajectory lengths (central bar indicates the median, bottom and top edges of the box indicate the 25th and 75th percentiles respectively and whiskers extend to the most extreme data points), generated as in Figure 2 from single particle signal of ER-targeted mEOS or Halo-tagged calreticulin labelled with 0.5 nM TRM-ligand. Note, the correlation between fluorophore photostability and trajectory length attest to the fidelity of the tracking procedure.



Supplementary Figure 2

Analysis of SPTs Diffusive dynamics and schematic illustration of internode and intranode motion.

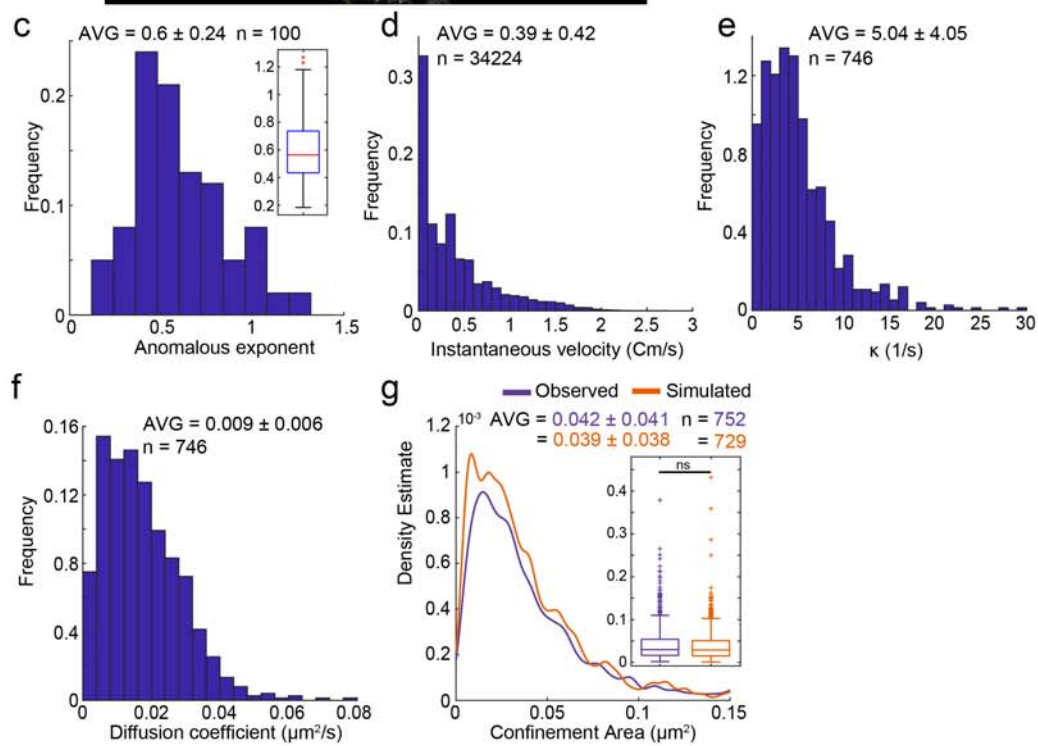
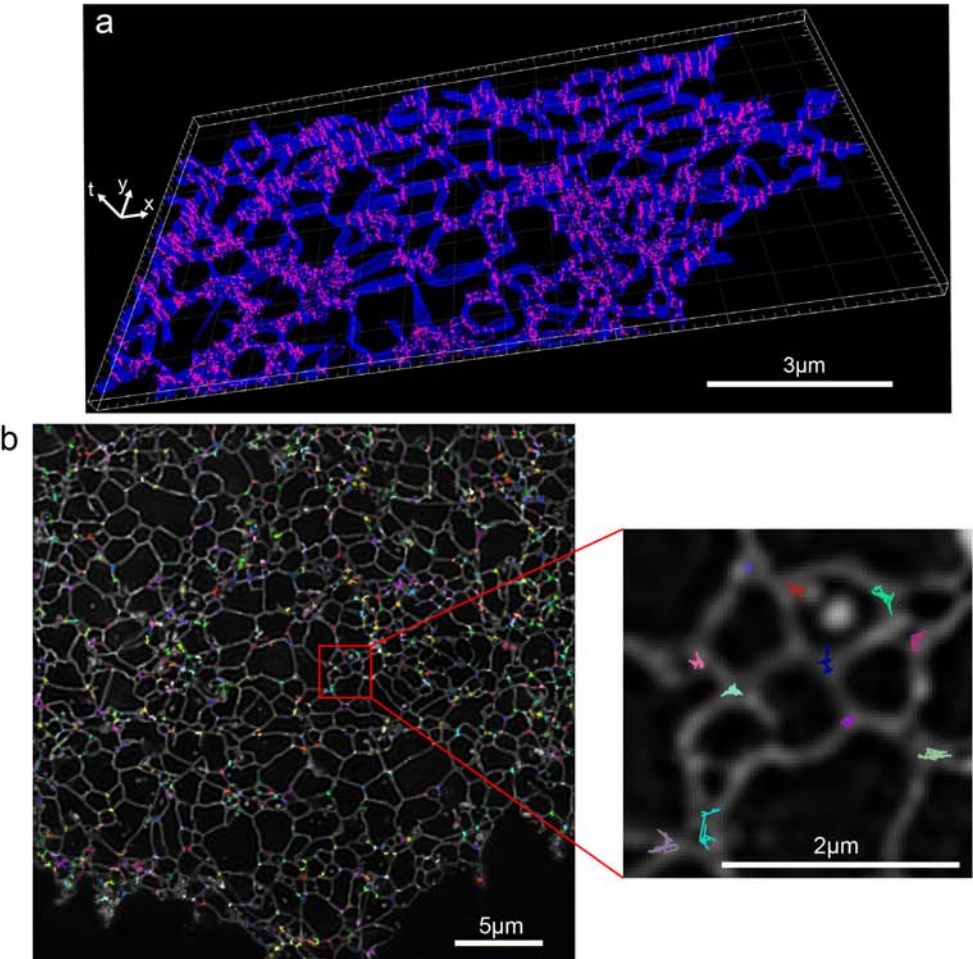
(a) Distributions of diffusion coefficients computed on the individual square bins presented in Fig.2f for the entire domain, including internode high-velocity displacements and intranode displacements. Numbers correspond to $\text{AVG} \pm \text{SD}$. (b) Mean Squared Displacement analysis applied on the SPTs from the experiment presented in Fig.2. Left panel: individual MSD curves color-coded by their anomalous exponent α and right panel: distribution of the corresponding anomalous exponents (central bar indicates the median, the bottom and top edges of the box indicate the 25th and 75th percentiles respectively and whiskers extend to the most extreme data points). (c) Average MSD computed on trajectory fragments contained in nodes. Left panel: average MSD curve for each node, color-coded according to its anomalous exponent and right panel: distribution of the corresponding anomalous exponents (central bar indicates the median, the bottom and top edges of the box indicate the 25th and 75th percentiles, respectively and whiskers extend to the most extreme data points). (d) Averaged MSD curves computed from trajectories exiting three different nodes with anomalous exponents $\alpha > 1$ indicative of a super-diffusive regime. For a description of the method, refer to Suppl. Note 1 section 1.1. (e) Synchronization procedure: **Left:** Trajectories are synchronized on their last point spent in the indicated node (red arrow). Trajectories can then either jump from node to node or move inside a node. **Right:** For each time τ after escaping the node, internode (red segments) and intranode (black segments) displacements (as identified from left panel) are grouped into separate ensembles and an average instantaneous velocity is computed for each group based on formula 35 and 36 (Suppl. Note 1); analysis performed on n trajectories as denoted in individual panels.



Supplementary Figure 3

Characteristics of ER luminal SPT displacements for several cell types and markers.

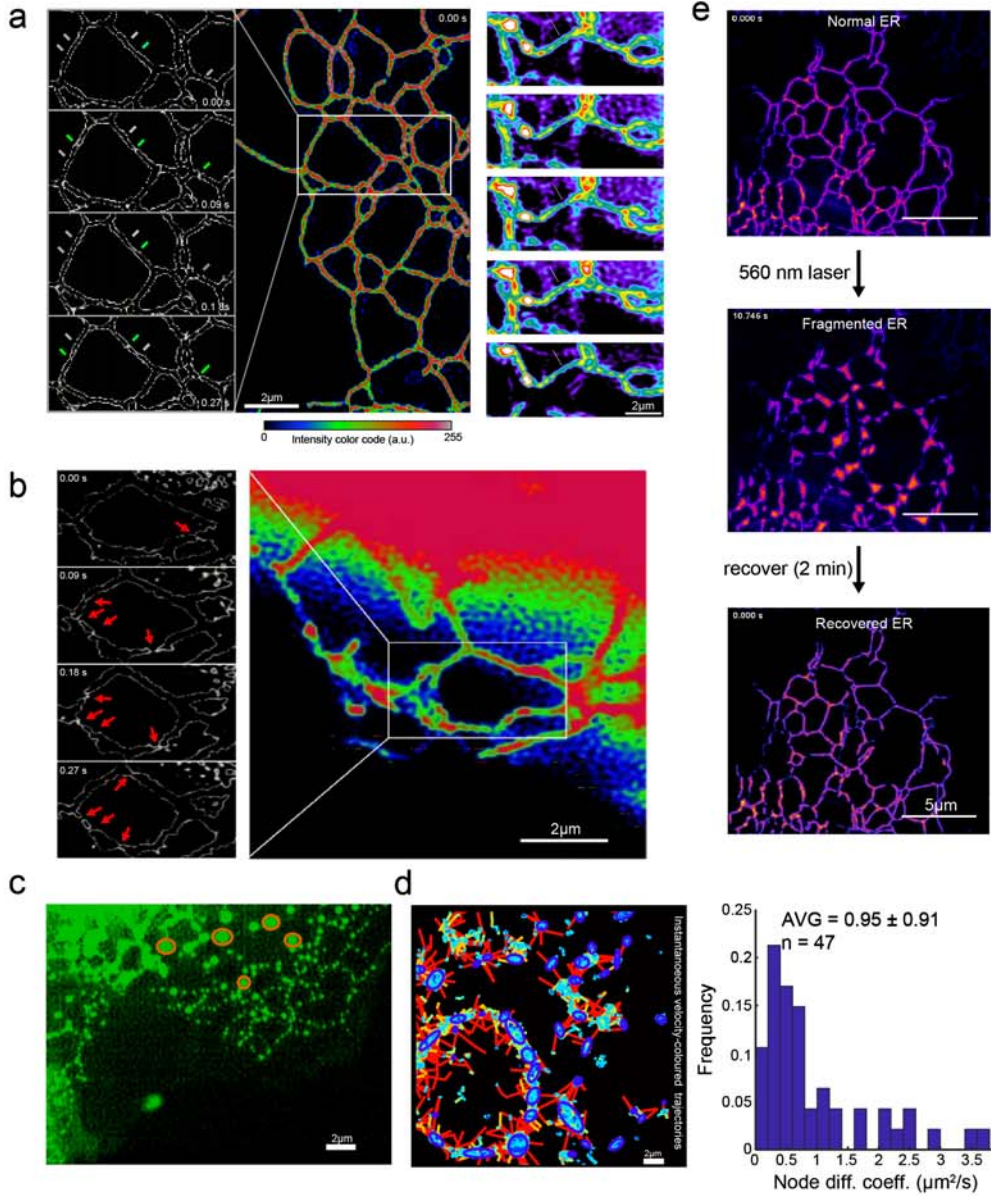
Statistics of SPTs motion obtained as in Fig.2, but for a HEK-293t cell (a) and a COS-7 cell (b) expressing an inert tracer – ER-targeted HaloTag with a C-terminal ER-retention signal, KDEL. Each column is organized similarly to Fig.2. Top: SPTs are presented color-coded according to the instantaneous velocity distributions presented below. The overlaid curves on the instantaneous velocity distributions correspond to the distributions expected for an exclusively diffusion-driven motion (solid lines, using the apparent D), or a combination of diffusion and flow (dashed lines, using D in nodes and the average instantaneous velocity between node). Inset are the corresponding cumulative distributions (color-coded as in the histogram). Middle: density and diffusion maps computed for a grid of square bins (sides of $0.2 \mu\text{m}$) imposed on the particle displacements and flow map computed by averaging the non-Brownian velocity jumps of particles moving between pairs of neighbour nodes and color-coded according to their velocity. Bottom: distributions of apparent diffusion coefficients (left), node diffusion coefficients (middle) and average instantaneous velocity between neighbouring nodes (right). (c) SPTs recorded for a COS-7 cell expressing an ER-localised TMR labeled Halo-tagged Calreticulin (left) color-coded according to the instantaneous velocity distribution (right). Overlaid curves on the histogram are as for (a-b). Shown are characteristic images observed in three independent repeats. All values are given as AVG \pm SD, for n trajectories as denoted in individual panels.



Supplementary Figure 4

Characteristics of ER structural components mobility.

(a) 3D kymograph presenting the motion of tubules and junctions across time (z-axis). (b) SPTs extracted from a stack of 50 images. Inset: magnification of an ER region showing junction trajectories. (c) Distribution of anomalous exponents obtained from SPTs (central bar indicates the median, the bottom and top edges of the box indicate the 25th and 75th percentiles, respectively and whiskers extend to the most extreme data). (d) Distribution of instantaneous velocities of the SPTs. (e-f) Estimation of the characteristics of the stochastic dynamics associated to the trajectories: distribution of spring constants (e) and diffusion coefficients (f). (g) Observed and simulated junctions confinement areas. Inset: corresponding boxplots (central bar indicates the median, the bottom and top edges of the box indicate the 25th and 75th percentiles, respectively and whiskers extend to the most extreme data points). A Man-Whitney U-test was used to compare the two distributions, returning a non-significant p-value ($p=0.1927$), see also video S5. (a,b) images are representative of three independent repeats. Analyses performed on n tubular junctions as denoted in individual panels.



Supplementary Figure 5

Contraction points in ER tubules and ER fragmentation.

High-speed Structured Illumination Microscopy (SIM) super-resolved images of the tubular ER for a COS7 cell (a) and a HEK293 cell (b), intensity color-coded. The observed contraction is unlikely to reflect Z-dimension tubule bending at a stiff angle, as sharp bending events have not been seen along the tubules in X-Y, and given the tubule dimensions the observed phenomenon is inconsistent with Z-bending at an angle sufficient to take a small tubule-fragment out of the focal plane. Tubule contractions are visible also in 3D-SIM (Video S9). (c) Confocal image of the ER, following 20 minutes exposure to 5 μ M Thapsigargin (an ER calcium uptake inhibitor). Note ER fragmentation accompanied by apparent tube-contraction, through elevation in cytoplasmic calcium²¹). (d) SPT velocity analysis, performed as in Fig. 2, of cell treated to induce ER fragmentation as in (c), values given as AVG \pm SD, n=47 nodes. Ovals exemplify the nearly spherical structures of fragmented ER. (e) Fragmentation, with notable contracted tubule intermediates, was induced by intense 561 nm laser illumination of cells expressing ER-targeted HaloTag and loaded with excess TRM. (a) characteristic images observed in five independent repeats, (b-e) characteristic images observed in three independent repeats.

1

2

3 **Supplementary Tables**
4
5
6
7
8
9
10
11
12
13

Supplementary Table 1: Single particle motion parameters across cell types, ER tracers.

D_{node} – diffusion coefficient in tubule junctions; V_{flow} – flow velocity in tubules, D_{app} – apparent diffusion coefficient computed from without diffusion/flow-deconvolution of single particle displacement profiles.

Supplementary Table 2: Plasmids list

Table 1

Cell type	Marker	D_app $\mu\text{m}^2/\text{s}$ AVG \pm SD	D_node $\mu\text{m}^2/\text{s}$ AVG \pm SD	v_flow $\mu\text{m}/\text{s}$ AVG \pm SD	n_Ttrajs/exp AVG	n
HEK 293T	Calreticulin	1.64 \pm 0.66	0.32 \pm 0.14	27.10 \pm 5.69	14177	7
	Halotag ER	1.70 \pm 0.94	0.39 \pm 0.08	26.97 \pm 6.36	11094	5
COS-7	Calreticulin	1.96 \pm 1.09	0.38 \pm 0.20	30.93 \pm 7.44	13485	6
	Halotag ER	3.94 \pm 1.03	0.57 \pm 0.29	42.72 \pm 2.32	13068	6
SH-SY5Y	Calreticulin	2.01 \pm 0.43	0.40 \pm 0.10	30.01 \pm 3.00	18789	4
	Halotag ER	2.59 \pm 0.65	0.42 \pm 0.19	31.70 \pm 3.42	12925	5

Table 1

Table 2

ID	Plasmid name	Description	Reference	First appearance	Label in figure
1081	pDendra2-ER-5	Mammalian expression, ER-localized Dendra2	Addgene plasmid #57716	Figure 1	Dendra2-ER
1578	mEos2-ER	Mammalian expression, ER-localized mEos2	PMID:19169260, Addgene plasmid #57373	Figure S1	mEos-ER
2158	ATeam1.03-nD/nA/pcDNA3	Mammalian expression of an ATP probe, A-Team	PMID:19720993, Addgene plasmid #51958	Figure 1	Ateam
2159	ER-Crowding_FRET1_CRH2_KDEL_pCDNA3.1(+)	Mammalian expression of FRET crowdedness probe	this study, based on PMID:25643150	Figure 1	ER Crowdedness FRET probe
2160	pFLAG_hCALR_kdel	Mammalian expression, of N-term. Halo-tagged human calreticulin	this study	Figure 2	HaloTag-Crt
1735	Hatolag_kdel	Mammalian expression of ER-localized HaloTag	this study	Figure S3	HaloTag-ER
UK1579	pmEos2-Calnexin-N14	Mamalian expression mEos2-tagged human calnexin	PMID:19169260, Addgene plasmid #57352	Figure 3	mEos2-calnexin

14 **Supplementary Videos**

15
16 Supplementary Video 1: Dendra2-ER photo conversion pulse chase.

17 Real time image series of experiment in figure 1e.

18
19 Supplementary Video 2: Raw data of ER single particle tame series.

20 Shown along super-resolution image reconstruction using single molecule localisation algorithm.

21
22 Supplementary Video 3: Zoom in on a particle with a long trajectory.

23 A magnified view that exemplifies a unidirectional displacement of a particle from Supplementary Video 2. Following
24 trajectories generation as in Figure 2, the view was filtered to show only trajectories with more 40 detection points.

25
26 Supplementary Video 4: Labeling control. SPT signal before, during and after the labeling.

27
28 Supplementary Video 5: ER structural components mobility.

29 High-speed Structured Illumination Microscopy (SIM) super-resolved time series of the tubular ER, shown alongside
30 skeletonised images of the network and statistics of tubule length frequency distribution.

31
32 Supplementary Video 6: Kinetic analysis of ER tubular network remodelling.

33 High-speed Structured Illumination Microscopy (SIM) super-resolved time series of the tubular ER. These are a sample of
34 the videos used to calculate a mean percentage of $0.14 \pm 0.04\%$ tubules growing at any given time. This was calculated
35 as the number of growing events per frame divided by the number of tubules per frame; for example.

36
37 Supplementary Video 7: Kinetic analysis of ER tubular network remodelling.

38 SIM images time series as in Supplementary Video 6, containing 80400 tubules in 100 frames (804 tubules per frame)
39 and 103 frames containing growing events (1.03 growing events per frame), giving $1.03/804 = 0.13\%$ of tubules growing
40 at any time.

41
42 Supplementary Video 8: Transient tubule narrowing.

43 Real time image series of experiment in figure 4F. Note that although the size of the tubule reduces slightly below the
44 resolution limit (80-90 nm), the contraction remains detectable due to a reduction in the intensity of the point-spread
45 function. Thus, applying the 'edges' colourmap (ImageJ), visualises a line of constant intensity, highlighting the contraction
46 phenomenon. The resolution limit precludes accurate distance measurements of contraction diameter.

47
48 Supplementary Video 9: 3D-SIM visualisation of tubule narrowing.

49 3D reconstruction of a stack of SIM images from paraformaldehyde/glutaraldehyde fixed cells.

50
51 Supplementary Video 10: ATP dependence of tubular contraction frequency.

52 High-speed SIM super-resolved time series images of individual ER tubules, with statistics of the number of point
53 contraction events per second shown alongside for ATP depletion conditions

54
55 Supplementary Video 11: Light-induced reversible ER fragmentation.

56 Realtime image series of experiment in figure S11.

57
58 Supplementary Note 1 : Mathematical modelling and analysis.

59 Details of the computational analyses of single particle tracking and structured illumination microscopy, and
60 their mathematical modelling.

61
62

Supplementary Information

Methods

1 Single Particles Trajectories analysis

When not stated otherwise, the following analysis was performed using MATLAB version 9.0 (MathWorks).

1.1 Mean Squared Displacement and first moment analysis

The Mean Squared Displacement (MSD) approach has been used to detect deviations from classical free diffusive motion of SPTs. Indeed, the MSD at time lag τ is defined by

$$MSD(\tau) = \langle |\mathbf{X}(t + \tau) - \mathbf{X}(t)|^2 \rangle, \quad (1)$$

where the average is computed either over realizations or time. This quantity is expected to grow like $MSD(\tau) = A\tau^\alpha$ where A is a coefficient and α is called the anomalous exponent. An exponent $\alpha > 1$ is a signature of a super-diffusive regime while $\alpha < 1$ indicates a sub-diffusive regime [1]. This analysis however does not provide any explanation for the mechanisms causing a specific regime because it is usually computed by averaging over time (time-averaged MSD) or space (trajectory-averaged MSD) thus disregarding the possible heterogeneous geometrical organization of STPs.

The motion exhibited by the recorded trajectories analyzed in Fig.2 is neither time nor space homogeneous. Indeed, the motion in nodes and tubules are different and trajectories exhibit high-velocity peaks of random duration (Fig.5d left), separated by random time intervals (Fig.5d right), making the MSD analysis hard to perform on these data. For that reason, we have chosen to conduct here an analysis based on the stochastic equation of motion (15) through which local parameters of motion are extracted from many redundant trajectories. This analysis allows to recover the field of force acting on the particles at each location from the first order moment of the individual trajectory displacements (16).

It is also possible to draw the same conclusions about the observed dynamics by conducting an MSD analysis on specific subset of trajectories.

For this analysis we relied on the time averaged MSD (taMSD) at time lag $\tau = 1 \dots (M_i - 1)$ defined, for a trajectory X_i composed of M_i points, as:

$$taMSD_i(\tau) = \frac{1}{M_i - \tau} \sum_{k=1}^{M_i - \tau} (X_i(t_{k+\tau}) - X_i(t_k))^2 \quad (2)$$

To recover the anomalous exponent from a taMSD curve, we fitted to the first 8 points of this curve in the log-log space the function:

$$\log(A) + \alpha \log(t) \quad (3)$$

using the `fit` function from MATLAB version 9.0 (MathWorks). Fig.S2b presents the taMSD curves in log-log space (left) and the corresponding anomalous exponents α (right) obtained by computing the taMSD on each trajectory, longer than 20 points (360ms) and visiting at least two reconstructed network nodes, from the experiment presented in Fig.2 and found a broad distribution of anomalous exponents ($0 \leq \alpha \leq 1.5$) in agreement the proposed two-states dynamics. To investigate the type of dynamics inside the nodes, we determined for each node the ensemble of N sub-trajectories $X_1 \dots X_N$ located inside the node and obtained the node MSD by averaging:

$$taMSD(\tau) = \frac{1}{N} \sum_{i=1}^N taMSD_i(\tau) \quad (4)$$

In Fig.S2c we report for each node of the experiment presented in Fig.2 its taMSD curve in log-log space (left) and the corresponding distribution of anomalous exponents (right) observing exponents $\alpha < 0.8$, indicating a sub-diffusive behavior. Finally, to investigate the type of dynamics outside nodes, we synchronized for each nodes, the trajectories on their exit from the node (as presented in section 1.7 and Fig.S2e) and computed an average MSD using eq.4. In Fig.S2d we present three examples of nodes for which this synchronization result in an averaged taMSD characterized by an anomalous exponent $\alpha > 1$ indicating in these cases a super-diffusive behavior.

1.2 Models for the instantaneous velocity distribution

1.2.1 Pure Diffusion model

To analyze the velocity histograms presented in Fig.2c,3a and S3, we use a two-dimensional random walk model:

$$\mathbf{X}(t + \Delta t) = \mathbf{X}(t) + \sqrt{2D\Delta t}\boldsymbol{\eta}, \quad (5)$$

where $\boldsymbol{\eta} = [\eta_1, \eta_2]$ with $\eta_1, \eta_2 \sim \mathcal{N}(0, 1)$ is a white noise. The distribution of the displacement lengths is given for $l > 0$ by [2]:

$$Pr_{\text{diff}} \left\{ \frac{\|\Delta \mathbf{X}(t)\|}{\Delta t} = l \right\} = \frac{l}{\sigma_d^2} \exp \left(\frac{-l^2}{2\sigma_d^2} \right), \quad (6)$$

where $\|\cdot\|$ is the Euclidean norm and

$$\sigma_d = \sqrt{\frac{2D}{\Delta t}}. \quad (7)$$

We use eq. 5, with the parameters presented in Table 1, using the apparent diffusion coefficient $D = D_{app}$ defined in section 1.4.2 to generate the distributions shown in Fig.2c, Fig.3a and S3 (solid lines).

1.2.2 Flow-diffusion switching model

To account for the fast (faster than the acquisition time $\Delta t = 18\text{ms}$) internode dynamics observed in Fig.2c, we use a jump-diffusion model [3] defined by the following rule

$$\mathbf{X}(t + \Delta t) = \mathbf{X}(t) + \begin{cases} \mathbf{J}\Delta t & \text{w. p. } \lambda\Delta t \\ \sqrt{2D\Delta t}\boldsymbol{\eta} & \text{w. p. } 1 - \lambda\Delta t \end{cases}, \quad (8)$$

where the statistics of the jumps \mathbf{J} is approximated from the observed flow velocity distribution, presented in the inset histogram of Fig.2g and in Fig.S3 as $\|\mathbf{J}\| \sim \mathcal{N}(\mu_{jump}, \sigma_{jump})$. Although the jump angle should follow the ER architecture, for the present model, we draw the angles from a uniform distribution in $[0, 2\pi]$. This simplification holds true as long as we are considering only the norm of the jumps. To estimate the distribution of displacement lengths of process 8, we use Bayes' law and condition the displacement on each state of the process:

$$\begin{aligned} Pr_{\text{switch}} \left\{ \frac{\|\Delta \mathbf{X}(t)\|}{\Delta t} = l \right\} &= Pr \left\{ \frac{\|\Delta \mathbf{X}(t)\|}{\Delta t} = l | \text{Jump} \right\} Pr\{\text{Jump}, t\} \\ &\quad + Pr \left\{ \frac{\|\Delta \mathbf{X}(t)\|}{\Delta t} = l | \text{Diff} \right\} Pr\{\text{Diff}, t\}. \end{aligned} \quad (9)$$

By definition the steady-state probability of being in a jump or diffusion state are:

$$\begin{aligned} Pr\{\text{Jump}\} &= \lim_{t \rightarrow \infty} Pr\{\text{Jump}, t\} = \frac{\lambda \Delta t}{1 - \lambda \Delta t + \lambda \Delta t} = \kappa. \\ Pr\{\text{Diff}\} &= 1 - Pr\{\text{Jump}\} = 1 - \kappa, \end{aligned} \quad (10)$$

where $\kappa = \lambda \Delta t \in [0, 1]$. Approximating eq. 9 by eq. 10 and replacing the displacement length distributions by a normal distribution for the jumps and a Rayleigh distribution (eq. 6) for diffusive displacements, we obtain

$$\begin{aligned} Pr_{\text{switch}} \left\{ \frac{\|\Delta \mathbf{X}(t)\|}{\Delta t} = l \right\} &= \kappa Pr \left\{ \frac{\|\Delta \mathbf{X}(t)\|}{\Delta t} = l | \text{Jump} \right\} + (1 - \kappa) Pr \left\{ \frac{\|\Delta \mathbf{X}(t)\|}{\Delta t} = l | \text{Diff} \right\} \\ &= \kappa \frac{1}{\sigma_j \sqrt{2\pi}} \exp \left(\frac{(l - \mu_{jump})^2}{2\sigma_{jump}^2} \right) + (1 - \kappa) \frac{l}{\sigma_d^2} \exp \left(\frac{-l^2}{2\sigma_d^2} \right), \end{aligned} \quad (11)$$

where σ_d is given by eq. 7. To estimate the switching probability κ in eq. 11, we use a Maximum-Likelihood Estimation (MLE) approach based on the probability

$$p(l|\kappa) = Pr_{\text{switch}} \left\{ \frac{\|\Delta \mathbf{X}(t)\|}{\Delta t} = l \right\}, \quad (12)$$

of observing l given κ . The MLE $\hat{\kappa}$ for N observed displacements l_1, \dots, l_N is [4]

$$\hat{\kappa} = \arg \max_{\kappa \in [0,1]} \sum_{i=1}^N \ln(p(l_i|\kappa)). \quad (13)$$

We compute $\hat{\kappa}$ using the `mle` function of MATLAB version 9.0 (MathWorks) applied to the trajectory displacements extracted from the SPTs described in methods.

To generate the distributions shown in Fig.2c and S3 (dashed lines), we use eq. 8, with the parameters presented in Table 1, using the diffusion coefficient in the nodes $D = D_{node}$ defined in section 1.4.3.

1.3 Reconstruction of the ER Network from SPTs

Detecting nodes (tubule junctions) boundary and inter-junction stretches (tubules) is based on the heterogeneity of the time-integrated particle spatial

density presented in Fig.2d and S3. The algorithmic procedure uses the large amount of recorded SPTs described in methods and proceeds as follows. We first construct clusters of points (nodes) defined as regions of aggregation of short displacements (aggregation regions appear to co-localize with short displacements as presented in Fig.2c and S3:

1. Define a threshold V_L (in $\mu\text{m}/\text{s}$), and discard from the analysis any point $X_i(t)$ such that $\frac{\|\Delta X_i(t)\|}{\Delta t} \geq v_L$ ($\Delta X_i(t)$ is the displacement as defined in methods).
2. Apply the `dbscan` [5] clustering algorithm to cluster the remaining points (implementation from `scikit-learn` [6] through Python3 provided by the Anaconda Distribution version 4.3.8 (Anaconda Inc.)).
3. Approximate the boundary of each cluster as an ellipse with semi-axes $a > b$ using a principal component analysis. Remove ellipses with an area $\pi ab > 4\mu\text{m}^2$ or an eccentricity $\frac{a}{b} > 4$. Merge overlapping ellipses by fitting a new ellipse to the union of their points.
4. Assign each points discarded in step 1 to the cluster corresponding to the ellipse in which they fall, if any.

The `dbscan` algorithm used in step 2 allows to generate clusters based on the local point density and requires two parameters:

1. The maximum distance R (in μm) below which two points are considered to be neighbors.
2. The minimum number of points N at a distance $\leq R$ of a point to start a cluster.

These two parameters define a minimal density $\frac{N}{R}$ of points/ μm^2 inside each cluster. The values of R and N depend on the morphology of the imaged ER and the local number of recorded trajectories. For each dataset, these values were determined empirically such that the computed clusters overlap with the ER structure formed by the trajectories.

Once nodes are found, we defined tubules by constructing a connectivity matrix C of size $K \times K$ (K number of detected nodes) where $c_{i,j}$ ($1 \leq i, j \leq K$) contains the number of trajectory displacements starting in node i and arriving in node j . Specifically, we increment the coefficient $c_{i,j}$ by one for each data point $X_k(t_l)$ ($1 \leq k \leq N_t$, $0 \leq l < M_k - 1$) in either of the following cases:

1. $X_k(t_l)$ is located in node i and $X_k(t_{l+1})$ in node j
2. $X_k(t_l)$ is located in node i , $X_k(t_{l+1})$ does not belong to any node and $X_k(t_{l+2})$ is located in node j (in this case $0 \leq l < M_k - 2$).

Finally, we removed from the graph any disconnected node. The different parameters used for reconstructing the graphs presented in the main text and supplementary data are given in Table 2. Graphs from Supplementary Table 1 (Main Text) were constructed using the parameter ranges: $V_L = [9, 19]\mu\text{m}/\text{s}$ (following the histogram of instantaneous velocities), $R = [0.08, 0.26]\mu\text{m}$, $N = [10, 45]$ points and $\pi ab \leq [4, 8]\mu\text{m}^2$. Ellipses representing the nodes of the graphs are shown in Fig.2d and S3.

1.4 Recovery of the local dynamics in the ER lumen from SPTs

1.4.1 Langevin equation and characteristics of motion

To interpret the individual trajectories described in methods, we use the classical overdamped limit of Langevin's equation [3, 7], where the velocity is the sum of a force or a flow (drift) plus a diffusion term. For a diffusion coefficient D and a field of force $\mathbf{F}(\mathbf{X})$, the dynamics is given by

$$\dot{\mathbf{X}}(t) = \frac{\mathbf{F}(\mathbf{X}(t))}{\gamma} + \sqrt{2D} \dot{\mathbf{w}}(t), \quad (14)$$

where $\dot{\mathbf{w}}(t)$ is a vector of independent standard δ -correlated Gaussian white noises and γ is the viscosity [3, 9]. The source of the driving noise $\dot{\mathbf{w}}(t)$ is the thermal agitation. To interpret trajectories, we coarse-grain eq. 14 in an effective stochastic process [10, 11, 12, 14]

$$\dot{\mathbf{X}}(t) = \mathbf{b}(\mathbf{X}(t)) + \sqrt{2} \mathbf{B}_e(\mathbf{X}(t)) \dot{\mathbf{w}}(t), \quad (15)$$

where $\mathbf{b}(\mathbf{X})$ is the empirical drift field, $\mathbf{B}_e(\mathbf{X})$ the diffusion related matrix and $\mathbf{D}_e(\mathbf{X}) = \frac{1}{2} \mathbf{B}_e(\mathbf{X}) \mathbf{B}_e^T(\mathbf{X})$ (T is the transposition) is the effective diffusion tensor. This model is used to construct the empirical estimators for the first and second order moments for the diffusion and drift from trajectories. The conditional moments are computed from the trajectory displacements (see methods) [9],

$$\mathbf{b}(\mathbf{X}) = \lim_{\Delta t \rightarrow 0} \frac{\mathbb{E}[\Delta X(t) | X(t) = \mathbf{X}]}{\Delta t}, \quad D_e(\mathbf{X}) = \lim_{\Delta t \rightarrow 0} \frac{\mathbb{E}[\Delta X(t)^T \Delta X(t) | X(t) = \mathbf{X}]}{2\Delta t}. \quad (16)$$

Here the notation $\mathbb{E}[\cdot | X(t) = \mathbf{X}]$ means averaging over all trajectories that are located at point \mathbf{X} at time t . The coefficients of eq. 15 can be statistically estimated from a large sample of trajectories in the neighborhood of the point \mathbf{x} at time t . On the recorded SPTs, the expectations in eq. 16 are estimated with a time step $\Delta t = 18ms$ according to the image acquisition time.

To compute the empirical drift and diffusion coefficients, we first partition the data into square bins $B(\mathbf{x}_k, r)$ of center \mathbf{x}_k and side $r = 0.2 \mu\text{m}$ [11]. Starting from the N_t acquired projected trajectories described in methods, eq. 16 becomes for a drift vector $\mathbf{b}(\mathbf{x}) = (b_x(\mathbf{x}), b_y(\mathbf{x}))$

$$\begin{aligned} b_x(\mathbf{x}_k) &\approx \frac{1}{N_k} \sum_{i=1}^{N_t} \sum_{0 \leq j < M_i - 1, \mathbf{X}_i(t_j) \in B(x_k, r)} \left(\frac{x_i(t_{j+1}) - x_i(t_j)}{\Delta t} \right) \\ b_y(\mathbf{x}_k) &\approx \frac{1}{N_k} \sum_{i=1}^{N_t} \sum_{0 \leq j < M_i - 1, \mathbf{X}_i(t_j) \in B(x_k, r)} \left(\frac{y_i(t_{j+1}) - y_i(t_j)}{\Delta t} \right), \end{aligned} \quad (17)$$

where N_k is the number of displacements starting in bin $B(x_k, r)$. Similarly, the components of the effective diffusion tensor $\mathbf{D}_e(\mathbf{x}_k)$ are approximated by the empirical sums

$$\begin{aligned} D_{xx}(x_k) &\approx \frac{1}{N_k} \sum_{i=1}^{N_t} \sum_{0 \leq j < M_i - 1, \mathbf{X}_i(t_j) \in B(x_k, r)} \frac{(x_i(t_{j+1}) - x_i(t_j))^2}{2\Delta t} \\ D_{yy}(x_k) &\approx \frac{1}{N_k} \sum_{i=1}^{N_t} \sum_{0 \leq j < M_i - 1, \mathbf{X}_i(t_j) \in B(x_k, r)} \frac{(y_i(t_{j+1}) - y_i(t_j))^2}{2\Delta t} \\ D_{xy}(x_k) &\approx \frac{1}{N_k} \sum_{i=1}^{N_t} \sum_{0 \leq j < M_i - 1, \mathbf{X}_i(t_j) \in B(x_k, r)} \frac{(y_i(t_{j+1}) - y_i(t_j))(x_i(t_{j+1}) - x_i(t_j))}{2\Delta t}. \end{aligned} \quad (18)$$

By definition, the moment estimators 17 and 18 are computed by averaging the displacements $\Delta X(t)$, each displacement contributing to the bin into which its initial point $X(t)$ falls. The computation reveals that the diffusion tensor is isotropic (Fig.2f and Fig.S3). Furthermore there is no need for further deconvolution of the SPTs, as the localization noise does not contribute until second order to the diffusion tensor and drift [13]. To obtain stable estimations, we only use bins that contain at least 20 displacements. We use the same grid to compute a density map, providing an estimate of the

local density of trajectories, by counting the number of displacements falling into each bin and dividing by the size of the square ($0.04\mu\text{m}^2$). Density and diffusion maps are presented in Fig.2df, Fig.3bc and Fig.S3a,b.

1.4.2 Estimation of the apparent diffusion coefficient

We define the apparent diffusion coefficient D_{app} as the diffusion coefficient estimated using the entire distribution of displacements. Note that this distribution also contains large values, that cannot be attributed to diffusion. We estimated D_{app} by averaging the values obtained using eq. 18 on each bin over the entire map (only for bins containing at least 20 points). The distribution of diffusion coefficients from individual bins of the diffusion map from Fig.2f is presented in Fig.S2a, in Fig.3d for the map of Fig.3c and in Fig.S3a,b for the other datasets.

1.4.3 Estimation of the diffusion coefficients in the nodes

The diffusion coefficient D_{node} inside each node is computed from eq. 16, but in addition we constrained both ends of the displacement be located inside the node. For a node delimited by an ellipse E , we get:

$$D_{node}(\mathbf{X}(t)) = \lim_{\Delta t \rightarrow 0} \frac{\mathbb{E}[\Delta X(t)^T \Delta X(t) | X(t) = \mathbf{X} \in E \text{ and } X(t + \Delta t) \in E]}{2\Delta t}. \quad (19)$$

We use eq. 19 to estimate the diffusion coefficient D_{node} in each node and report their distributions in Fig.2f (inset) for the main text dataset and Fig.S3a,b.

1.4.4 Estimation of the internodes displacements

We define the instantaneous velocity (in $\mu\text{m}/\text{s}$) between two successive points of the same trajectory $\mathbf{X}(t_1)$ and $\mathbf{X}(t_2)$ ($t_2 > t_1$) as the ratio of the distance to elapsed time

$$v(\mathbf{X}(t_1), \mathbf{X}(t_2)) = \frac{\|\mathbf{X}(t_2) - \mathbf{X}(t_1)\|}{t_2 - t_1}, \quad (20)$$

where $\|\cdot\|$ is the Euclidean distance. We define the flow velocity v_{flow} between two nodes A and B , as the average of the instantaneous velocities for the

displacements connecting the two nodes:

$$v_{flow}(A, B) = \mathbb{E} \left[v(\mathbf{X}(t_1), \mathbf{X}(t_2)) \middle| \begin{array}{l} (\mathbf{X}(t_1) \in A, \mathbf{X}(t_2) \in B) \text{ or} \\ (\mathbf{X}(t_1) \in B, \mathbf{X}(t_2) \in A) \end{array} \right], \quad (21)$$

where by construction $t_2 - t_1 \in \{\Delta t, 2\Delta t\}$ (see tubule reconstruction from section 1.3). We discretize eq. 21 and obtain the estimator:

$$v_{flow}(A, B) \approx \frac{1}{N} \sum_{i=1}^N v(\mathbf{X}_i(t_1), \mathbf{X}_i(t_2)), \quad (22)$$

where N is the number of trajectory displacements connecting the nodes A, B and \mathbf{X}_i is the i^{th} such displacements. The velocity v_{flow} characterizes the jump flow between nodes. As shown in Fig.2c, this internode flow is associated with the thick tail of the velocity distribution. The distributions of jump velocities between each pair of neighbor nodes for the different datasets are presented in Fig.2g and Fig.S3a,b.

1.5 Static ER network analysis

1.5.1 Flow directionality and strongly connected components

To determine whether the ensemble of observed displacements between two neighbor nodes i and j form a uni- or bi-directional flow, we define a unidirectionality score r as the ratio of the number of observed displacements between the two nodes with direction $i \rightarrow j$ divided by the total number of displacements in both directions:

$$r_{i,j} = \frac{c_{i,j}}{c_{i,j} + c_{j,i}}, \quad (23)$$

where C is the connectivity matrix of the graph as defined in section 1.3. Using $r_{i,j}$, we build a binary version C' of C defined as

$$c'_{i,j} = \begin{cases} 1 & \text{when } r_{i,j} \geq 0.25 \\ 0 & \text{otherwise} \end{cases}. \quad (24)$$

C' has the property that $c'_{i,j} = c'_{j,i} = 1$ when $0.25 \leq r_{i,j} \leq 0.75$ (bi-directional flow) and $c'_{i,j} = 1, c'_{j,i} = 0$ when $r_{i,j} > 0.75$ (uni-directional flow). The ratio $r_{i,j}$ (and thus $c'_{i,j}$) is computed only for pairs of nodes connected by at least

three displacements ($c_{i,j} + c_{j,i} \geq 3$). To find the connected components of the reconstructed network, we use the classical Tarjan Strongly Connected Components (SCCs) detection algorithm [15] on the binary connectivity matrix C' (`graphconncomp` function from MATLAB version 9.0 (MathWorks)). SCCs are a partition of the ensemble of nodes such that there exists a path (taking into account the directionality) from each node of a subset to any other node of the same subset. The presence in Fig.4b of a SCC encompassing almost the entire graph shows that the observed flows have the potential to move particles through almost the entire network. In addition Fig.4b also displays the flows directionality on the links as: arrows for uni-directional, solid (no arrow) for bi-directional and dashed for undecided.

1.5.2 Count of Afferent and Efferent branches

We further characterize the structure of the reconstructed ER graph by computing for each node k the number of afferent and efferent branches connected to it. An afferent (resp. efferent) branch is a link $l \rightarrow k$ (i.e. $c_{l,k} > 0$) (resp. $k \rightarrow l$, $c_{k,l} > 0$) where l is any other node of the graph. Based on the count of afferent and efferent nodes, we define the out and in-degree of node k using the connectivity matrix C as:

$$\text{outdeg}(k) = \sum_{i=1}^N \mathbb{1}_{c_{k,i}>0} \quad \text{and} \quad \text{indeg}(k) = \sum_{i=1}^N \mathbb{1}_{c_{i,k}>0}, \quad (25)$$

where $\mathbb{1}_{a>b} = \begin{cases} 1 & \text{if } a > b \\ 0 & \text{otherwise} \end{cases}$, and N is the number of nodes in the graph.

In- and out-degrees are computed only for nodes k such that $\sum_{i=1}^N c_{i,k} > 2$ and $\sum_{i=1}^N c_{k,i} > 2$ respectively. The distribution of in- and out-degrees are presented in Fig.4c.

1.5.3 Fraction of entering and exiting displacements in nodes

To study the passing dynamics of trajectories through nodes we define a retention score for the nodes defined as the ratio of the number of exiting displacements to the total number of entering and exiting displacements for

a node k :

$$\phi_k = \frac{\sum_{i=1}^N c_{k,i}}{\sum_{i=1}^N c_{i,k} + \sum_{i=1}^N c_{k,i}}, \quad (26)$$

where C is the connectivity matrix of the graph and N the number of nodes. We have $\varphi \in [0, 1]$ such that $\varphi_k \rightarrow 0$ indicates that the node retains trajectories, $\varphi_k \rightarrow 1$ indicates that trajectories originate from this node and $\varphi_k \approx 0.5$ indicates that trajectories pass through the node. φ_k was computed only for nodes k such that $\sum_{i=1}^N c_{k,i} + c_{i,k} > 2$. The distribution of ϕ for the reconstructed ER network is shown in Fig.4d.

1.6 Transient ER network analysis

At steady-state, we identified the uni- and bi-directional flows inside tubules (Fig.4b), we now investigate how the direction of these flows evolve with time. To this end, we determine the distribution of durations of uni-directionality periods of the flow between two nodes as presented in Fig.5a. The analysis is performed on each pair of neighbouring (directly linked by trajectories) nodes, linked by at least 20 displacements registering one of the two possible directionalities (either node $A \rightarrow B$ or $B \rightarrow A$). The following algorithm groups the successive displacement events as a function of their directionality and determine the duration of these groups:

1. Collect the next displacement event observed at time t_{first} , identify its direction say $A \rightarrow B$ and form a new group containing this event.
2. Accumulate in the group created in step.1 the following jump events with direction $A \rightarrow B$ and stop when there are no more event or after encountering two events with direction $B \rightarrow A$ (in this case the event or the two successive $B \rightarrow A$ events when it occurs, are not collected). The last event considered in the group occurs at time t_{end} and always has the same direction as the group (see Fig.5a).
3. Compute the duration of the group as $\tau = t_{\text{end}} - t_{\text{first}}$.
4. Return to step 1.

We discarded groups formed by less than 3 displacements with the same direction. The distribution of the uni-directional flow durations τ is presented in Fig.5b.

To interpret the mean of this distribution, we recall that this statistics is partly contaminated by the fraction of activated particles located in nodes and the track lengths. Indeed, only photo-activated particles appear in the statistics. To recover the uni-directional duration of the fluxes from the empirical distribution, we use a model taking into account these two characteristics. The probability that the flux between nodes A and B lasts a duration $\tau_{Uni} = t$ is computed by conditioning on having k events (k particles flowing in the same direction) during that time

$$Pr\{\tau_{Uni} = t\} = \sum_{k=1}^{\infty} Pr\{\tau_1 + \dots + \tau_k = t | k\} Pr_{Uni}\{k\}, \quad (27)$$

where the probability that k event occurs in the same direction is by symmetry,

$$Pr_{Uni}\{k\} = \frac{1}{2^k} \quad (28)$$

and τ_k is the arrival time of the k^{th} event after the first one. We consider that the distributions of arrival times are Poissonian with same rate λ , independent of the initial node A or B . We conclude that

$$Pr\{\tau_1 + \dots + \tau_k = t | k\} = \lambda \frac{(\lambda t)^{k-1}}{(k-1)!} \exp(-\lambda t). \quad (29)$$

Computing the sum from eq. 27, we obtain for at least 2 events

$$Pr\{\tau_{Uni} = t\} = \frac{\lambda}{2} \left(\exp\left(-\frac{\lambda t}{2}\right) - \exp(-\lambda t) \right). \quad (30)$$

Eq. 30 is the probability density function when all particles are labeled and its average is $\frac{3}{2\lambda}$. When a particle is activated with probability p , which represents the steady-state fraction of labeled particles, the statistics of uni-directional flow is still given by formula 30 but with a rate $\tilde{\lambda}$. Using Bayes' law, the probability of observing a displacement event is

$$\begin{aligned} Pr\{\tau_{Uni} = t\} &= Pr\{\tau_{Uni} = t, activated\} Pr\{activated\} \\ &\quad + Pr\{\tau_{Uni} = t, not activated\} Pr\{not activated\}, \end{aligned} \quad (31)$$

where $\Pr\{\text{activated}\} = p$ is the fraction of activated molecules. The second term is zero because we cannot see displacement events from non-activated molecules. Thus the mean unidirectional flow duration becomes

$$\langle \tau \rangle = p\bar{\tau}, \quad (32)$$

where the rates are related by $\lambda = p\tilde{\lambda}$. Considering a fraction $p = 1\%$ of activated molecules, we predict that the mean undirectional time should be around $\langle \tau \rangle = 38ms$ instead of the observed $\bar{\tau} = 3.89s$.

1.7 Instantaneous velocities along individual trajectories

To obtain statistics of the velocity fluctuations of trajectories (recorded at different times over a period of seconds) and possibly located either in tubules or nodes, we introduced a 'synchronization' procedure: the velocity fluctuations of individual trajectories were monitored starting from the last time point where the particle was in a given node prior to its exit. The velocity fluctuations following the node exit was plotted as a function of time elapsed since the synchronization event (a universal time scale for all trajectories regardless when they were detected). In details, the synchronization event is defined for a trajectory X_i , its last recorded point inside some node A ,

$$t_i^* = \max_{0 \leq j < M_i - 1} \{X_i(t_j) \in A \text{ and } X_i(t_{j+1}) \notin A\}. \quad (33)$$

Considering the n_A trajectories going through node A , the ensemble of last points inside A is

$$X_A = \{X_i(t_i^*) | i = 1..n_A\}. \quad (34)$$

We now divide displacements along individual trajectories into two subsets based on the starting node A and appearing at a time $\tau > 0$ after exit: $X_{A,\text{node}}(\tau)$ containing displacements inside nodes and $X_{A,\text{tubule}}(\tau)$ containing displacements connecting two nodes:

$$\begin{aligned} X_{A,\text{node}}(\tau) &= \{X_i(t_i^* + \tau) | X_i(t_i^*) \in X_A \text{ and } X_i(t_i^* + \tau - \Delta t) \in N \text{ and } X_i(t_i^* + \tau) \in N\} \\ X_{A,\text{tubule}}(\tau) &= \{X_i(t_i^* + \tau) | X_i(t_i^*) \in X_A \text{ and } X_i(t_i^* + \tau - \Delta t) \in N_1 \text{ and } X_i(t_i^* + \tau) \in N_2\}, \end{aligned}$$

where $N, N_1, N_2 \in \mathcal{N}$ the ensemble of nodes and $N_1 \neq N_2$ (N_1 or N_2 can be not a node). We computed the average velocities $v_{Inter}(\tau)$ (resp. $v_{Intra}(\tau)$) at time $\tau \geq \Delta t$ for each subset:

$$v_{Intra}(\tau) = \frac{1}{n_{A,intra}(\tau)} \sum_{\mathbf{X}_i(t_i^* + \tau) \in X_{A,node}(\tau)} v(\mathbf{X}_i(t_i^* + \tau - \Delta t), \mathbf{X}_i(t_i^* + \tau)) \quad (35)$$

and

$$v_{Inter}(\tau) = \frac{1}{n_{A,inter}(\tau)} \sum_{\mathbf{X}_i(t_i^* + \tau) \in X_{A,tubule}(\tau)} v(\mathbf{X}_i(t_i^* + \tau - \Delta t), \mathbf{X}_i(t_i^* + \tau)), \quad (36)$$

where $n_{A,intra}(\tau)$ (resp. $n_{A,inter}(\tau)$) is the number of displacements from synchronized trajectories that fall inside (resp. between two nodes) at time τ and $v(.,.)$ is the instantaneous velocity (eq. 20). The synchronization process and the intra and inter node velocities along synchronized trajectories are presented schematically in Fig.S2e. In this figure, schematic trajectories synchronized on their exit of a node A are presented on the left panel and their associated instantaneous velocity as a function of the time since exit τ from A are presented on the right panel. Fig.5c presents the average (line) and standard deviation (shade) of the instantaneous velocity for v_{intra} (black) and v_{inter} (red) for a selected node A of the main-text network for $\tau \leq 0.2s$.

1.8 Instantaneous velocity peaks duration and inter-peaks period

To further analyze the fluctuations of the instantaneous velocities along individual trajectories we proceed as in section 1.7 and synchronize the trajectories leaving a given node A. We then estimated the time spent by individual trajectories in a high velocity regime (above a threshold $v_{high} = 19\mu m/s$) as the number of successive time steps $\tau = j\Delta t$ ($j = 0\dots$) for which

$$v(X_i(t_i^* + \tau + j\Delta t), X_i(t_i^* + \tau + (j+1)\Delta t)) > v_{high}, \quad (37)$$

where X_i is a synchronized trajectory and $v(.,.)$ is the instantaneous velocity (eq. 20). The distribution of the high velocity regime durations is shown in Fig.5d and the distribution of periods between two high velocity regimes in Fig.5e, computed for trajectories synchronized for each node of the ER-network. Note that we considered only trajectories that visited at least three different network nodes.

1.9 Dynamics of tubular junctions

1.9.1 Extraction of junctions from SIM images

We extracted the features of tubular junctions from a SIM images stack (50 images) through a procedure similar to [16]: first, the contrast of the entire image stack was manually modified to make the ER network more apparent. Then each image was skeletonized, junctions were extracted from the skeleton [17] (AnalyzeSkeleton plugin, ImageJ) and only junctions covering more than 3 pixels were kept. For each image of the stack, a new grayscale image was generated where only the pixels belonging to selected junctions appear white and afterward a Gaussian blur with $\sigma = 1\text{px}$ was applied to produce a single-particle like image. On this stack of grayscale images, we applied a particle detection and tracking algorithm [8] to follow junctions through successive images (Spot Detection and Tracking plugins, Icy). This procedure produces an ensemble of N trajectories $X_1 \dots X_N$ such that $X_i = X_i(t_0) \dots X_i(t_{M_i})$ and $\Delta t = t_i - t_{i-1} = 90\text{ms}$. From this ensemble, we keep only trajectories possessing at least 40 points. These trajectories are displayed in Fig.S4ab overlaid on top of the average stack image.

1.9.2 Mean Squared Displacement (MSD) analysis

We first characterize the type of diffusive motion exhibited by trajectories using a Mean Squared Displacement (MSD) analysis. For an ensemble of T trajectories the MSD at time t_k is defined as:

$$MSD(t_k) = \frac{1}{T} \sum_{i=1}^T \|X_i(t_k) - X_i(t_0)\|^2 \approx A(t_k - t_0)^\alpha \quad (38)$$

where $\|.\|$ is the Euclidean distance, A is a coefficient and $\alpha > 0$ is the anomalous exponent characterizing the type of diffusive motion. To estimate α , we fit the first 20 points of the MSD curve to the line $y(t_k) = \log(A) + \alpha \log(t_k - t_0)$ in the log-log space using a MATLAB version 9.0 (MathWorks) script. Fig.S4c shows the distribution of α obtained applying this procedure to 100 independent samples of $T = 20$ randomly selected trajectories from the ensemble of trajectories possessing at least 40 points and keeping only the fits for which the coefficient of determination $R^2 > 0.75$. We found that $\alpha = 0.60 \pm 0.24$ suggesting a sub-diffusive behavior or diffusion in the presence of confinement forces [19].

1.9.3 Confined motion of tubular junctions

The distribution of instantaneous velocities (Fig.S4d) suggests to model junction's dynamics as a diffusion process confined by active forces generated by a parabolic potential well. The corresponding equation of motion is expressed as an Ornstein-Uhlenbeck stochastic process

$$\dot{X} = \kappa(X - \mu) + \sqrt{2D}\dot{\mathbf{w}}, \quad (39)$$

where μ is the center of the potential well, κ in $1/s$ the spring coefficient, D in $\mu\text{m}^2/\text{s}$ the diffusion coefficient and $\dot{\mathbf{w}}(t)$ is a vector of independent standard δ -correlated Gaussian white noises. We estimate for each recorded trajectory X_i the three parameters: $\hat{\mu}_i$, $\hat{\kappa}_i$ and \hat{D}_i . The center of the well μ_i is approximated by the center of mass of the trajectory:

$$\hat{\mu}_i = \frac{1}{M_i} \sum_{j=0}^{M_i-1} X_i(t_j). \quad (40)$$

The parameters $\hat{\kappa}_i$ and \hat{D}_i are estimated using the maximum-likelihood estimators [18]. For a trajectory $X_i(t_0) \dots X_i(t_n)$ we compute for each dimension $X_i(t) = (x_i^1(t), x_i^2(t))$, $d = 1, 2$

$$\begin{aligned} \hat{\beta}_1^d &= \frac{n^{-1} \sum_{k=1}^n x_i^d(t_k) x_i^d(t_{k-1}) - n^{-2} \sum_{k=1}^n x_i^d(t_k) \sum_{k=1}^n x_i^d(t_{k-1})}{n^{-1} \sum_{i=1}^n x_i^d(t_{k-1})^2 - n^{-2} (\sum_{i=1}^n x_i^d(t_{k-1}))^2} + \frac{4}{n}, \end{aligned} \quad (41)$$

$$\begin{aligned} \hat{\beta}_2^d &= \frac{n^{-1} \sum_{k=1}^n (x_i^d(t_k) - \hat{\beta}_1^d x_i^d(t_{k-1}))}{1 - \hat{\beta}_1^d}, \end{aligned} \quad (42)$$

$$\begin{aligned} \hat{\beta}_3^d &= n^{-1} \sum_{k=1}^n (x_i^d(t_k) - \hat{\beta}_1^d x_i^d(t_{k-1}) - \hat{\beta}_2^d (1 - \hat{\beta}_1^d))^2, \end{aligned} \quad (43)$$

from which we obtain the estimators:

$$\hat{\kappa}_i^d = \frac{\log(\hat{\beta}_1^d)}{\Delta t} \quad \text{and} \quad \hat{D}_i^d = \frac{\hat{\kappa} \hat{\beta}_3^d}{1 - (\hat{\beta}_1^d)^2} \quad (44)$$

where $\Delta t = t_k - t_{k-1}$ is the time-step and the term $\frac{4}{n}$ in $\hat{\beta}_1^d$ is a correction for the low number of points. In practice, we obtain a symmetric tensor and

force field computed as the averages:

$$\hat{\kappa}_i = \frac{\hat{\kappa}_i^1 + \hat{\kappa}_i^2}{2} \quad \text{and} \quad \hat{D}_i = \frac{\hat{D}_i^1 + \hat{D}_i^2}{2}. \quad (45)$$

We apply this estimation only on trajectories possessing at least 40 points. Fig.S4e shows the distribution of the estimated spring constants $\hat{\kappa}$ and Fig.S4f the distribution of the estimated diffusion coefficients \hat{D} .

1.9.4 Estimating the area of confinement of tubular junctions

In this section, we define and compute the area of confinement of each junction based on the statistics of the trajectories. For each trajectory X_i we compute the 95% confidence ellipse $e_i = (c_i, a_i, b_i, \varphi_i)$ of center c_i , largest (resp. smallest) semi-axis a_i (resp. b_i) and angle (with x-axis) φ_i , of the spatial spreading of its points, considering this distribution as normal. We obtained the ellipse as follows [20]: first, we collected all points $X_i(t)$ of the trajectory into a $2 \times n$ matrix O^i , then applied a Singular Value Decomposition algorithm to the covariance matrix of O^i : $U^i \Sigma^i (V^i)^* = \text{cov}(O^i)$ and finally recovered the ellipse as:

$$c_i = \frac{1}{M_i} \sum_{j=0}^{M_i-1} X_i(t_j), \quad a_i = \sqrt{5.991\sigma_{1,1}^i}, \quad b_i = \sqrt{5.991\sigma_{2,2}^i}, \quad \varphi_i = \arctan\left(\frac{u_{2,1}^i}{u_{1,1}^i}\right), \quad (46)$$

where $\sigma_{1,1}^i$ and $\sigma_{2,2}^i$ are the two eigenvalue of the matrix $\text{cov}(O^i)$. We define the confinement area A_i for a trajectory X_i as the area of the estimated ellipse: $A_i = \pi a_i b_i$. The distribution of observed confinement areas is presented in Fig.S4g.

We now compare this distribution, with the expected distribution for a particle moving in a potential well. To this end for each trajectory X_i , we simulated eq. 39 with the estimated parameters $\hat{\mu}_i, \hat{\kappa}_i, \hat{D}_i$ using Euler's scheme to obtain a trajectory Y_i :

$$Y_i(t_k) = Y_i(t_{k-1}) + \hat{\kappa}_i(Y_i(t_{k-1}) - \mu_i)\delta t + \sqrt{2\hat{D}_i\delta t} \boldsymbol{\eta}, \quad (47)$$

where $\delta t = 0.0001\text{s}$ is the simulation time-step, $\boldsymbol{\eta} = [\eta_1, \eta_2]$ with $\eta_1, \eta_2 \sim \mathcal{N}(0, 1)$ is a white noise and $Y_i(t_0) = \mu_i$. To prevent the choice of the first point to influence the statistics, we run the simulation for 45000 time steps before recording the trajectory. We then sub-sampled Y_i by keeping one

every 900 points to match the experimental acquisition time $\Delta t = 0.09$ s and computed the confinement area of Y_i using the same procedure as for X_i . This procedure was only applied to junctions for which $\hat{\kappa}_i > 0$. The distribution of confinement areas obtained from simulated trajectories is shown in Fig.S4g.

2 Characterization of ER tubule contractions

2.1 Extraction of tubule contraction statistics

Fast SIM images of ER in live cells, acquired and reconstructed as described in methods, were rendered using the Edges look-up-table of the Fiji software, with contrast settings to visualise one-pixel wide boundaries of the tubules. Contraction sites were identified as such if the tubule edges bended to merge more than once at the same position. In Fig.5g we report the distributions of three observable characteristics of contraction events extracted from SIM images. The duration of a contraction event (Fig.5g left) is computed as the difference between the last and first frames for which the event is detected; The time interval between successive contractions (Fig.5g middle) is computed for each individual tubule and pair of successive contraction events as the difference between the first frame of the second contraction and the last frame of the first contraction; Finally the length of a contraction (Fig.5g right) is computed by counting the number of pixels along the tubule axis involved in the contraction.

2.2 Elementary model of tubule contraction

The relation between the ER constrictions inside the tubules and the flow is suggested rather than correlative. To increase the evidences of this correlation, we propose an elementary computation to link the contractions and flow. Considering an incompressible ER luminal fluid, the conservation of the mass is

$$\frac{\partial \rho}{\partial t} = \operatorname{div}(\mathbf{v}\rho), \quad (48)$$

where ρ is the fluid density and \mathbf{v} the velocity at position \mathbf{x} . When a constriction occurs, we suppose that it leads to a decreased volume V_c , that generates a local flow. This flow can be obtained by integrating eq. 48 inside

the tubule and we get:

$$\frac{dV}{dt} = S_2 v_2 - S_1 v_1, \quad (49)$$

where S_2, S_1 are the cross-sections at the right and left of the constriction associated with a constant velocity v_1 (resp. v_2) on the surface (note that we assume that there is no flow through the lateral surface of the tubule). When $S_2 = S_1$, we obtain since $v_2 = -v_1$ (by symmetry), so that the initial flow is given during the constriction phase by

$$v = \frac{1}{2S_1} \frac{dV}{dt}. \quad (50)$$

Thus a constriction occurring in a cylinder of constant section πr^2 along a segment of size $L = 300$ nm during $15ms$, leads to a velocity $V = 0.3/0.03 = 10\mu m/s$. To recover the velocity at the junction, we need now to model how this change in the tubule shape contributes to the velocity of ejection v_{expelled} .

A possible model is that the flow enters the node through a smaller section than the radius of the tubule. Suppose that the size is $r = 0.5r_{\text{tub}}$, then using the mass conservation with this ratio of surfaces, we obtain a velocity at the entrance of a junction of

$$v_{\text{entrance}} = \frac{S_1}{S_{\text{entrance}}} v, \quad (51)$$

leading to a factor 4. Thus we obtain a velocity that could reach $v_{\text{entrance}} = 40\mu m/s$, compatible with the maximum velocity we find for the ejection of trajectories (Fig.2).

If the cross-section in the node at the two opposite tubules from the one where the flow is generated are identical to the one receiving the flow, we finally get the relation

$$v_{\text{expelled}} = \frac{v_{\text{entrance}}}{2} \approx 20\mu m/s. \quad (52)$$

Fig.5h illustrates the consequence of a constriction: a local constriction generates a flow v in both directions. The flow leads to an acceleration at the entrance of a tubule, if the entrance has a small surface. Due to the flow conservation, the velocity of the expelled trajectory is of the order $20\mu m/s$. Considering a pinch length of $L = 100$ nm we obtain $v \approx 3\mu m/s$, $v_{\text{entrance}} = 13\mu m/s$, $v_{\text{expelled}} = 7\mu m/s$ while for $L = 400$ nm we obtain $v \approx 13\mu m/s$, $v_{\text{entrance}} \approx 53\mu m/s$ and $v_{\text{expelled}} = 27\mu m/s$.

2.3 Simultaneous contractions statistics

Under the assumption that contractions are spatio-temporally independent events, the probability of a contraction follows a Poissonian distribution of rate λ such that

$$P\{\text{one contraction in } [t, t + \Delta t]\} = \lambda \Delta t \quad (53)$$

Thus the probability of n contractions during that time interval is a rare event which probability is given by

$$\begin{aligned} P\{n \text{ contractions in } [t, t + \Delta t]\} &= (P\{\text{one contraction in } [t, t + \Delta t]\})^n \\ &= (\lambda \Delta t)^n. \end{aligned}$$

Considering $\lambda = 1/f_{contraction}$ where $f_{contraction} = 1.5\text{Hz}$ as given in Fig.5f during a time step of $\Delta t = 100\text{ms}$ (the acquisition time of SIM images), then $P\{\text{one contraction in } [t, t + \Delta t]\} = 0.15$ and $P\{\text{two contractions in } [t, t + \Delta t]\} = 0.0225$ and thus can be neglected compared to one contraction.

3 Tables

	Pure Diffusion Model	Flow-Diffusion Model
Dataset 1 (Main text)	$D_{app} = 1.13 \mu\text{m}^2/\text{s}$	$D_{node} = 0.19 \mu\text{m}^2/\text{s}$ $\mu_j = 22.9 \mu\text{m}/\text{s}$ $\sigma_j = 6.92 \mu\text{m}/\text{s}$ $\kappa = 0.33$
Dataset 2 (Fig.S3a)	$D_{app} = 1.02 \mu\text{m}^2/\text{s}$	$D_{node} = 0.35 \mu\text{m}^2/\text{s}$ $\mu_j = 23.19 \mu\text{m}/\text{s}$ $\sigma_j = 3.85 \mu\text{m}/\text{s}$ $\kappa = 0.31$
Dataset 3 (Fig.S3b)	$D_{app} = 4.10 \mu\text{m}^2/\text{s}$	$D_{node} = 0.57 \mu\text{m}^2/\text{s}$ $\mu_j = 45.01 \mu\text{m}/\text{s}$ $\sigma_j = 12.75 \mu\text{m}/\text{s}$ $\kappa = 0.41$

Table 1: Estimated motion parameters of the pure diffusion and flow-diffusion models for the datasets presented in the main text and supplementary figures.

Symbol	Description	Datasets		
		Main text	Fig.S3a	Fig.S3b
V_L	Max. inst. vel. ($\mu\text{m}/\text{s}$)	9.5	10	19
R	Max. neighbor distance (μm)	0.1	0.12	0.18
N	Min. num. points in cluster	25	35	30

Table 2: Parameters used for fitting the network on the presented datasets.

References

- [1] Metzler R. and Klafter J. (2000). "The random walk's guide to anomalous diffusion: a fractional dynamics approach", Physics reports, 339(1), 1-77.
- [2] Michalet X. (2010). "Mean Square Displacement Analysis of Single-Particle Trajectories with Localization Error: Brownian Motion in Isotropic Medium", Phys. Rev. E, 82.4: 041914.
- [3] Z. Schuss (2010). "Diffusion and Stochastic Processes: an Analytical Approach", Springer, New York,.
- [4] Kendall M. and Stuart A. (1961). "The advanced theory of statistics: Inference and relationship", Hafner Publishing, New York
- [5] Ester M., Kriegel H. P., Sander J. and Xu X. (1996). "A density-based algorithm for discovering clusters in large spatial databases with noise", Kdd Vol. 96, No. 34, pp. 226-231.
- [6] Pedregosa F., Varoquaux G., Gramfort A., Michel V., Thirion B., Grisel O., Blondel M., Prettenhofer P., Weiss R., Dubourg V., Vanderplas J., Passos A., Cournapeau D., Brucher M., Perrot M. and Duchesnay E. (2011). "Scikit-learn: Machine Learning in Python", Journal of Machine Learning Research.
- [7] Langevin P. (1908). "Sur la théorie du mouvement Brownien", C.R. Paris, 146, 530–533.
- [8] Chenouard N., Bloch I. and Olivo-Marin, J.C. (2013). "Multiple hypothesis tracking for cluttered biological image sequences", IEEE transactions on pattern analysis and machine intelligence, 35(11), 2736-3750.
- [9] Hoze N. and Holcman D. (2017). "Statistical Methods for Large Ensembles of Super-Resolution Stochastic Single Particle Trajectories in Cell Biology", Annual Review of Statistics and Its Application.
- [10] Holcman D., Hoze N. and Schuss Z. (2015). "Analysis and interpretation of superresolution single-particle trajectories", Biophysical journal, 109 (9), 1761-1771.

- [11] Hoze N., Nair D., Hosy E., Sieben C., Manley S., Herrmann A., Sibarita J.B., Choquet D. and Holcman D. (2012). "Heterogeneity of receptor trafficking and molecular interactions revealed by superresolution analysis of live cell imaging", Proc. Natl. Acad. Sci. USA, 109: 17052–17057.
- [12] Hoze N. and Holcman D. (2014). "Residence times of receptors in dendritic spines analyzed by stochastic simulations in empirical domains", Biophysical journal 107 (12), 3008-3017
- [13] Hoze N. and Holcman D. (2015). "Recovering a stochastic process from super-resolution noisy ensembles of single-particle trajectories", Physical Review E 92 (5), 052109 2015.
- [14] Hoze N. and Holcman D. (2017)."Statistical Methods for Large Ensembles of Super-Resolution Stochastic Single Particle Trajectories in Cell Biology", Annual Review of Statistics and Its Application, (4):189-223.
- [15] Tarjan R. (1972). "Depth-first search and linear graph algorithms", SIAM vol. 1, no 2, p. 146-160.
- [16] Nixon-Abell J., Obara J. C., Weigel V. A., Li D., Legant R. W., Shan Xu C., Pasolli A., Harvey K., Hess F.H., Betzig E., Blackstone C. and Lippincott-Schwartz J. (2016). "Increased spatiotemporal resolution reveals highly dynamic dense tubular matrices in the peripheral ER", Science, 354.
- [17] Arganda-Carreras I., Fernandez-Gonzalez R., Munoz-Barrutia A. and Ortiz-De-Solorzano C. (2010), "3D reconstruction of histological sections: Application to mammary gland tissue", Microscopy Research and Technique, Volume 73, Issue 11, pages 10191029.
- [18] Tang C.Y. and Chen S.X. (2009). "Parameter estimation and bias correction for diffusion processes", Journal of Econometrics, vol. 149, p. 65-81.
- [19] Amitai A., Seeber A., Gasser S.M. and Holcman D. (2017). "Visualization of chromatin decompaction and break site extrusion as predicted by statistical polymer modeling of single-locus trajectories.", Cell Reports, 18(5), 1200-1214.

- [20] Bishop C.M. (2006), "Pattern recognition and machine learning", Springer.
- [21] McKinney S.A., Murphy C.S., Hazelwood K.L., Davidson M.W., Looger L.L. (2009), "A bright and photostable photoconvertible fluorescent protein", Nature Methods, 6(2), 131.